2015-03-01

Three-Dimensional Flow Measurements Around a Mechanical Flapping Wing

Eric R. Hardester

Brigham Young University - Provo

Three-Dimensional Flow Measurements Around a

Mechanical Flapping Wing

Eric R. Hardester

A thesis submitted to the faculty of
Brigham Young University
in partial fulfillment of the requirements for the degree of

Master of Science

Tadd T. Truscott, Chair
Steven E. Gorrell
Julie Crockett

Department of Mechanical Engineering

Brigham Young University

March 2015

ABSTRACT

Three-Dimensional Flow Measurements Around a
Mechanical Flapping Wing

Eric R. Hardester
Department of Mechanical Engineering, BYU
Master of Science

Man has always been fascinated by the flight of birds and insects. First attempts at flight involved flapping wings to mimic the birds and insects that had been observed in flight. Fixed wings proved to be a more practical approach and have been used for over 100 years for manned flight. Emphasis has been placed on flapping wing designs for micro air vehicles (MAVs) as research has shown that challenges arise in lift generation and stability in fixed wing flight as the scale decreases [1].

This research explores the use of 3D, time-resolved, Synthetic Aperture PIV (SAPIV) in measuring flow velocities on the mechanical flapping wing of a MAV in tethered flight. The vortical structures on the MAV are measured using both SAPIV and 2DPIV to be able to analyze 2D and 3D velocity fields. The 3D vorticity plots and 2D slice vorticity plots show the three-dimensional nature of the Leading Edge Vortex (LEV) and Trailing Edge Vortex (TEV). 2DPIV plots and 2D slices from the 3D data show general agreement in the structure and behavior of the flow around the flapping wing.

The lift and thrust generated by the MAV are measured using a force gauge. The wing tip is tracked in 2D and 3D for synchronization of the measured lift forces with the flow field measurements from the SAPIV. The positive and negative circulation are plotted against the measured lift and thrust forces.

The measured lift and thrust forces from the force gauge are then compared to the calculated lift and thrust forces from the measured 3D circulation found through the SAPIV flow field measurements. A plane measured parallel to the LEV and TEV vortex cores allows the defining of a unit vector that is directed normal to the top of the wing and the LEV and TEV cores. The decomposition of the unit vector allows for the calculation of the lift and thrust generated by the circulation around the wing. The comparisons between the measured and calculated forces show good agreement in the case of the measured and calculated lift forces.

Keywords: flapping flight, 3DPIV, 2DPIV, leading edge vortex, trailing edge vortex, LEV, TEV

ACKNOWLEDGMENTS

TABLE OF CONTENTS

LIST OF TABLES

LIST OF FIGURES

CHAPTER 1.   INTRODUCTION

1.1   MAVs and Flapping Flight

Man has always been fascinated by the flight of birds and insects. First attempts at flight involved flapping wings to mimic the birds and insects that had been observed in flight. Fixed wings proved to be a more practical approach and have been used for over 100 years for manned flight. As unmanned air vehicles (UAVs) have become more prevalent, the size of manmade flying machines has decreased. Emphasis has been placed on flapping wing designs for micro air vehicles (MAV) as research has shown that challenges arise in lift generation and stability in fixed wing flight as the scale decreases [1]. Alternatively, rotary wings, as stated by Clemons et al., "offer good agility and vertical-take-off-and landing (VTOL) capability, [but] suffer from wall-proximity effects, are too noisy, and usually are inefficient for low Reynolds number flight" [2]. Flapping flight has its own challenges, namely recreating the kinematics of a flapping wing, but allows for greater lift generation and stability at small scales and low Reynolds numbers ($Re < 10,000$) [1,2].

When flow passes by a fixed wing, the lift force generated is limited by the separation of flow as the angle of attack increases [3], creating unsteady flow in the wake behind the wing. The flow in the wake consists of von Karman vortex streets [4] and wingtip vortices [3]. The vortex streets are an indication of drag on fixed wing aircraft, and wings are often designed to minimize such drag effects. The wingtip vortices on fixed wings also increase drag by wasting energy in the generation of vortices that do not provide additional lift or thrust. In contrast, a flapping wing translates and rotates, reversing the direction of the vortex streets to generate thrust [2] and augmenting the wingtip vortices to generate lift [5].

Shyy et al. observed "a leading edge vortex (LEV), a trailing edge vortex (TEV), and a tip vortex (TiV)" in the flow around a flapping wing of a computational hawkmoth model [1]. An example of an LEV, TEV, and TiV on a downward flapping wing can be seen in Figure 1.1. The LEV is attached to the leading edge of the wing, and the TEV is attached to the trailing edge of

the wing. An LEV is apparent through the entire cycle of flapping on insect wings. It has been observed that the LEV is formed during the upstroke and downstroke of a flapping period and stays attached to the wing as the wing translates and rotates through a fluid and is shed during the transitions between upstroke and downstroke [6]. The presence of the LEV increases the lift generated by the wing, allowing birds and insects to fly. Shyy et al. documented TEVs and TiVs being present on the wing surface [1]. In fixed wing flight, TiVs decrease lift and induce drag while in flapping flight, TiVs can sometimes promote lift by connecting the TEV and LEV together in a complete loop [7]. While LEVs, TEVs, and TiVs remain attached to the wing surface, a "draining" process has been observed, allowing the LEVs, TEVs, and TiVs to interact in the near wake of a flapping wing. The draining process is exhibited as spanwise flow along the leading edge in the direction of the wing tip. These interactions are thought to contribute to the lift produced by a flapping wing through the low pressure cores that are generated [4].
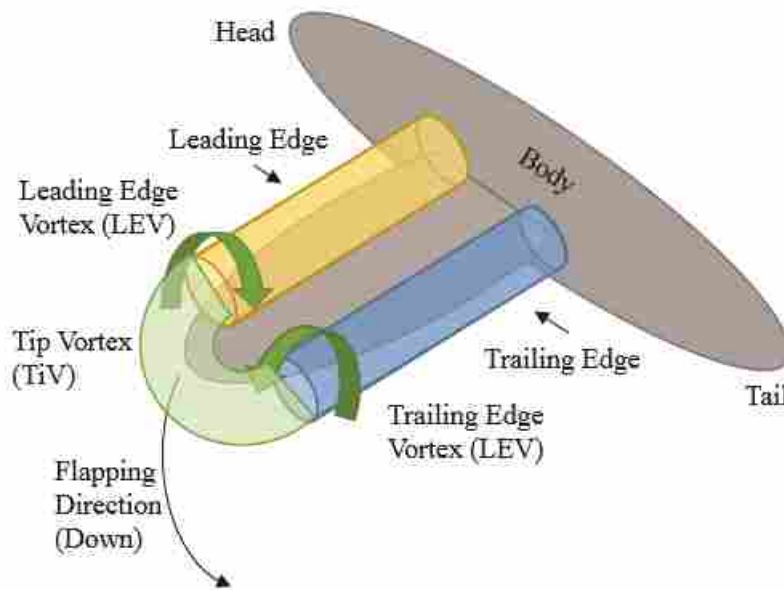
Figure 1.1: A diagram showing the Leading Edge Vortex (LEV) and Trailing Edge Vortex (TEV) locations on a flapping wing during a downward flap.

Many studies involve mimicking the wings and wing trajectories of birds or insects. The hawkmoth is a common insect used to study the mechanics of flapping flight [7]. Experiments performed in air and oil [8] often focus on the wing surfaces and the near wake, and data can be

2

collected during starts and after long time periods [9]. Research is focused on understanding the flow structures on and around the wings that facilitate lift in an effort to design MAVs to utilize those structures for greater lift.

The two critical numbers for understanding the flow around a flapping wing are the Reynold's number and Strouhal number

$$Re = \frac{\rho V L}{\mu}, \qquad St = \frac{f L}{V},$$

where ρ is the density of the fluid, L is the characteristic length, μ is the dynamic viscosity, and f represents the flapping frequency. The Reynolds number gives a the ratio of the inertial forces over the viscous forces. The Strouhal number describes oscillating flow mechanisms, like flapping wings. The Strouhal number provides a measure of the efficiency of propulsion using flapping mechanisms by giving a ratio of the amount of flapping required for a forward velocity. It has been found that most birds, insects, and aquatic animals have Strouhal numbers in the range of 0.2-0.4 at cruising speeds ($100 < Re < 100,000$). The Reynolds and Strouhal numbers are used for proper scaling of flapping mechanisms in relation to insects and birds.

Currently, research is being done on finding optimum wing profiles and wing trajectories for mechanical wings [10]. To increase understanding of the flow structures present around mechanical flapping wings, we are studying a commercially available MAV - the iFly Vamp [11]. The iFly Vamp measures 25.4 cm long, has a 30.5 cm wingspan. The Vamp is powered by a small electric motor that drives a pivoting mechanism at the front edge of the wings, with the back edge of the wings pinned. A strut forms the leading edge of the wings with the rest of the wings made of a thin, plastic membrane. Steering is accomplished by moving the pinned back edges of the wings up or down, depending on the direction of the turn. The mechanism is controlled wirelessly through a simple remote. Stability is achieved through a fixed tail section connected to the back of the body of the MAV (Figure 1.2). It should be noted that the MAV only achieves marginal stability during flight.

1.2   Flow Visualization

Several techniques are widely used to visualize the flow around flapping wings. The first is the use of smoke or dye to visualize the pathlines and swirling motions of a fluid around a flapping

3
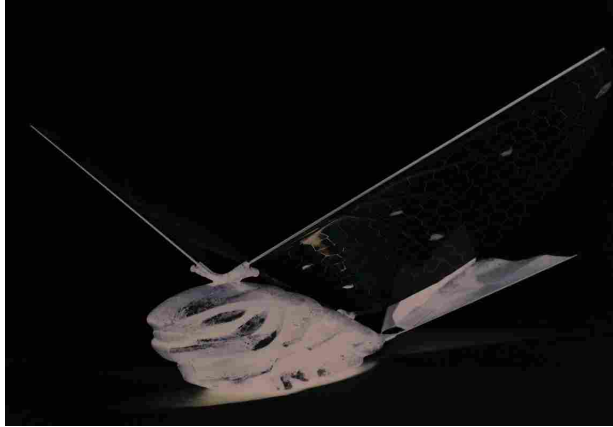
Figure 1.2: An image of the iFly Vamp. The Vamp is powered by an electric motor that drives a pivoting mechanism at the front edge of the wings, with the back edge of the wings pinned to the body.

wing [12]. This helps to get a broad picture of what the flow is doing. This technique is mainly limited to qualitative analysis.

The other widely used technique in flow visualization of flapping wings is particle image velocimetry (PIV). PIV is accomplished using a high speed camera and a high power source of light, usually a pulsing laser. The flow around the object of interest, in this case the wing, is seeded with small particles. The laser is focused into a thin sheet parallel to the camera and illuminates the particles in the flow. A camera is used to capture images in quick succession. The images are then processed in pairs by tracking groups of particles in the image pairs using a method called cross-correlation. The first image is segmented into "windows" containing particles, and a search is performed on the second image for windows with the greatest correlation to the windows in the first image. In general, the greater the density of particles in the windows, the more precise the correlation. The cross-correlation provides the displacement of the groups of particles in each window that has occured in the time between the two images (See Figure 1.3). A velocity field is created by knowing the time dt between images and the distance the groups of particles move in each image pair, allowing analysis of the wake structures and forces in the flow around the wing. The density of the velocity vector field is determined by the final window size used for correlation. More information about how to perform PIV experiments can be found in Raffel et al. [13].

A problem that arises in using PIV to visualize the flow around a flapping wing is that while the wake structures of a flapping wing are 3-dimensional, the light sheet used in PIV limits the

4
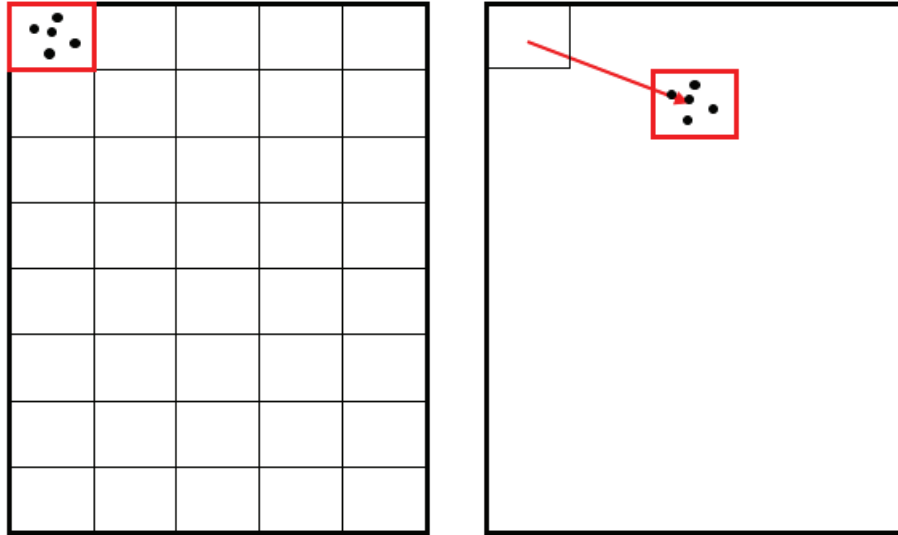
Figure 1.3: In PIV image processing, a cross-correlation is performed on an image pair. The first image is segmented into "windows" of particles. A search is performed on the second image for windows with the greatest correlation to the windows from the first image. The cross-correlation provides a measure of the displacement and change in time for particle movement.

data collected to 2-dimensions. Several "slices" of the flow are acquired by moving the light sheet through the volume of interest, both in the spanwise direction along the wing [14] and chordwise direction from the leading edge to the trailing edge [4]. This helps to give a better representation of the 3-dimensional flows around the wing, but leaves an incomplete picture because of areas not imaged between the slices and only measures 2 components of the velocity.

Stereo PIV has been used to achieve 3-dimensional, 3-component (3D-3C) time-resolved data through phase-locking techniques [8]. The use of Stereo PIV can provide multiple 2D-3C slices of a particular moment in the phase which could be combined and interpolated to obtain a 3D-3C velocity field. Having a phase-locked time-resolved reconstruction of the 3D-3C velocity field offers a better understanding of the wake structures working on the wing than does a 3D-2C field provided by 2DPIV.

Recently, Bomphrey et. al used a technique called Tomographic PIV to obtain instantaneous velocity fields in volumes [15]. Using four cameras, a thin volume of interest was captured. By taking images of the volume of interest at constant time intervals, a view of the flow structures in the wake behind a desert locust were visualized. With tomographic PIV, more data is gathered than with Stereo PIV because of the use of an imaging volume instead of imaging planes. How-

ever, combining instantaneous volumes from tomographic PIV causes a few problems. Bomphrey et al. reported small discontinuities present in the data from combining the instantaneous volumes from wake deformation in the time interval between image pairs [15].

Synthetic Aperture PIV (SAPIV) shows promise as a new means of capturing instantaneous 3D-3C data for flapping wings. Belden et al. present SAPIV as a method for capturing full 3D-3C velocity fields of a flow volume with greater spatial resolution than other 3DPIV techniques [16]. SAPIV is based on light field imaging. An array of cameras is focused on a volume of interest. Because each camera sees the volume of interest from a different angle, it is possible to see particles that are partially occluded by other particles in the other camera views. The images from each of the different cameras are overlapped and digitally refocused. This gives an out of plane viewing area on the same scale as the viewing window with similar spatial resolutions. The use of SAPIV can help researchers overcome the challenges associated with 2DPIV of flapping wings and provide greater detail than Stereo PIV. This greater detail comes from the aquisition of instantaneous velocity fields in a fluid volume instead of capturing phase-locked velocity fields in several parallel planes and interpolating the data [14].

1.3 Research Objectives

The objectives of my research were two fold. The first was to expand the knowledge of the fluid dynamics around flapping wings by acquiring 3D instantaneous flow field measurements using SAPIV. The results of the SAPIV experiments performed represented the first known 3D instantaneous flow field measurements of a flapping wing. The second objective was to expand the use of SAPIV in experimental fluid dynamics. As a relatively new PIV technique, the use of SAPIV helped to improve the robustness of the SAPIV code, as well as explore further the limits and possibilities with SAPIV.

1.4 Overview

In the following chapters, I will present the methods and results of the experiments performed on the MAV. Through experimentation and anlysis, we have made attempts at and succeeded, according to the results, in deciphering the forces associated with and flow fields around

the flapping wing of the MAV while tethered. The data was gathered through 2DPIV and SAPIV techniques and through direct force measurements. The results contain comparisons between the flow field measurements and the force measurements.

Chapter 2 covers the methods used for experimentation and analysis. The methods used for the SAPIV and 2DPIV are outlined with discussion of the experimental setup as well as the data processing techniques. The process of gathering the force measurements and matching those measurements with wing position is also discussed.

Chapter 3 contains an article published by Kenneth R. Langley, Tadd R. Truscott, Scott L. Thomson, and myself. The article, "Three Dimensional Flow Measurements on Flapping Wings Using Synthetic Aperture PIV", was received April 27th, revised August 25th, and published in *Experiments in Fluids* online in October 2014 [17]. This paper is divided into two sections, with the first covering the results of SAPIV performed on painted lady butterflies and the second section covering the results of the 2DPIV and SAPIV performed on the MAV. The paper also presents the force measurements from the MAV and the comparision between the force measurements and the measured positive and negative circulation from the flow fields aqcuired using SAPIV. My contribution to the paper was all the information presented about the MAV. All of the MAV flow field and force measurement experiments, results, and analysis was done by me. The butterfly experiments performed by Ken are beyond the scope of this thesis.

Chapter 4 contains further results obtained from the experiments performed with more analysis of the measured forces and flow field data. The vorticity and circulation results from the SAPIV experiments are used to estimate the lift and thrust generated by the wing. The measured lift and thrust are compared to the estimated lift and thrust from the flow fields, representing the first known estimation of the lift and thrust generated by a flapping wing from 3D instantaneous flow field measurements. The measured lift and estimated lift profiles show good agreement, and reasons for the differences in the measured thrust and estimated thrust are discussed.

CHAPTER 2.   METHODS

There are two experimental setups associated with the MAV. The first experimental setup is for the 2DPIV and SAPIV data acquisition. The second setup is for the horizontal and vertical force data acquisition.

2.1   Flow Field Measurements

2.1.1   SAPIV

The first objective was to identify the flow structures around the flapping wing of a MAV. An acrylic box was manufactured for studies of the iFly Vamp (the MAV). This box was 0.60 x 0.60 x 0.45 m^3 in volume. It was made from 1/8" cast acrylic sheets that were bonded using a solvent-cement. The box consisted of 5 sides, with the bottom 0.60 x 0.60 m^3 side left open for access to the MAV and for seeding the air inside the box with particles. The clear acrylic walls provided unobstructed views for the cameras. An array of eight Photron SA-3 Fastcams was used for imaging the fluid flow. The volume of interest was illuminated by an expanded laser beam of an Nd:YLF laser. It was expanded to give a viewing volume of 100 mm x 100 mm x 100 mm (Figure 2.1).

The MAV was held in place by a pair of beaker clamps connected to a magnetic base. The base was connected to a steel sheet placed inside the box. This provided a firm mount for the testing of the MAV.

Seeding of the flow was performed with Expancel Micro-hollowspheres. The hollowsphere particles had a mean diameter of 40 μm and a density of 25 kg/m3 (Expancel, 461 DET 40 d25). The particles were placed inside the box near an edge. The particles were then dispersed using compressed air. 10 seconds were allowed after dispersion of particles to allow for a more even
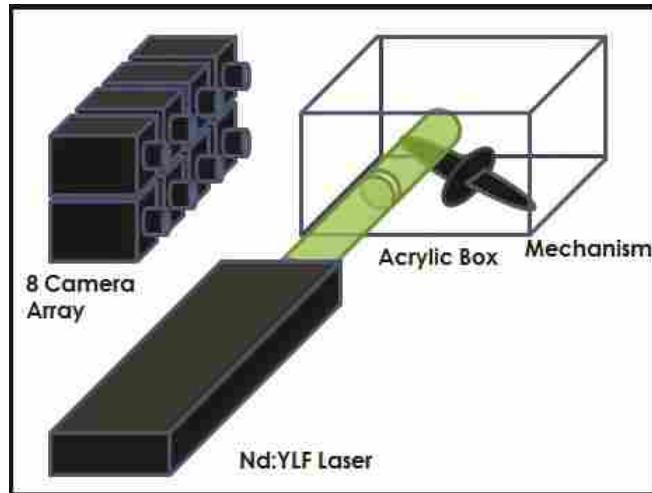
Figure 2.1: An array of 8 high-speed cameras will image the flow around the Vamp in an acrylic box using an expanded laser for illumination of the volume of interest.

distribution of particles in the volume as well as allow the fluid motion caused by the compressed air to dissipate.

The volume was illuminated with a Quadtronix Darwin Duo 552 nm laser. The laser was equiped with a beam expander, allowing the beam to be expanded to a maximum diameter of 10 cm. The illuminated volume was large enough to illuminate most of the right wing of the MAV. All experimental runs were performed on the right wing of the MAV.

The cameras were attached to an aluminum frame designed for performing SAPIV. The cameras were arranged with 4 cameras on the upper portion of the frame and 4 cameras on the lower portion of the frame. Each camera lens center was approximately 0.13 m from the neighboring camera lenses on each row, and the upper camera lens centers were approximately 0.32 m from the lower camera lens centers. The camera array was placed such that the camera lenses were parallel to and 0.81 m from the center plane of the MAV.

The syncronization of the cameras and laser was accomplished with a pulse generator. The experiment was controlled with 3 pulse signals, a trigger pulse and 2 laser pulses, as seen in Figure 2.2. The trigger signal was set to pulse every 4 ms to syncronize the camera shutters with the pulse generator clock. The cameras were connected together so that all camera shutters were synchronized with each other at 1000 Hz, so the cameras received a pulse from the pulse generator for every 4 images collected. The laser received two pulse signals, or one pulse signal for each

9

laser shutter. The first laser shutter pulse was set to pulse at 0.8 ms after the trigger pulse, and again 2 ms after the first pulse. The second laser shutter pulse was set to pulse at 1.2 ms after the trigger pulse, and again 2 ms after the first pulse. The spacing between the two laser pulse triggers established a dt of 0.4 ms between images in each image pair. The 2 ms between each pair of laser pulses set the time between each image pair at 2 ms. A delay was programmed into the pulse generator to allow the laser to warm up before beginning each experimental run.
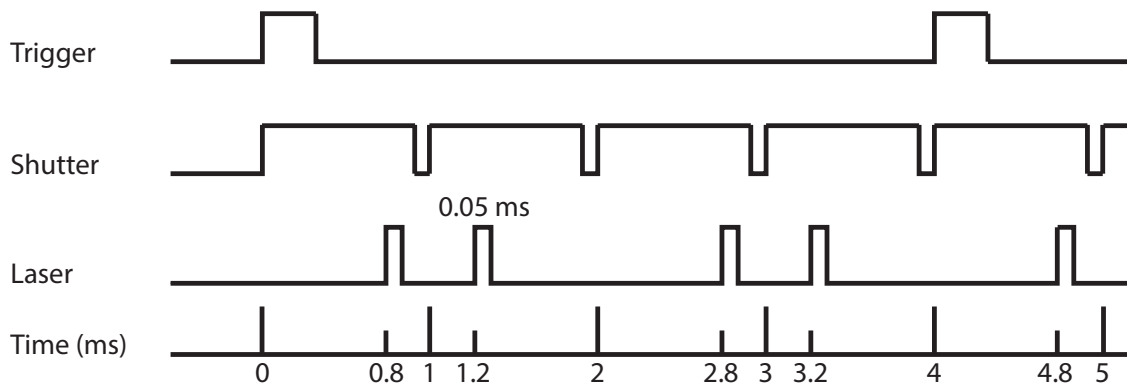
Figure 2.2: The laser and cameras are controlled by a pulse generator. A trigger pulse is created every 4 ms. The trigger signal is connected to the highspeed cameras and syncs the shutters (1000 fps) with the pulse generator clock. The laser receives two signal pulses, one for each laser beam. The first beam is triggered at 0.8 ms for 0.05 ms with a 2 ms delay between each pulse. The second beam is triggered at 1.2 ms for 0.05 ms with a 2 ms delay between each pulse. The first laser shutter pulse occurs just before the camera shutters close and the second laser beam pulse occurs right after the camera shutters open again. The two laser pulses provide a dt of 0.4 ms within each image pair and 2 ms between image pairs.

The density of the particles in the SAPIV experiments, measured in particles per pixel (ppp) was calculated using two different methods. The first method involved counting all of the connected components in a single raw image. The total count for particles in a single image taken from a center camera was 6130 particles, with a density of 0.0166 ppp. The second method counted all of the connected components within the thresholded and reconstructed volume. The total count of particles in the reconstructed volume was 43,931 particles with a density of 0.000833 ppp. The lower density in the reconstructed volume was expected, as particles are lost in the thresholding step of reconstruction of the volume. Both the first and second method results suggest that the particle seeding density was low, due to the difficulty in seeding the air around the MAV. Higher

density seeding (> 0.05 ppp) in larger volumes of interest, such as in this experiment, is still being investigated and could improve the spatial resolution of the 3DPIV [16].

The overall uncertainty of the SAPIV velocity measurements was 0.3243 m/s, or $\pm 11\%$ velocity error and was calculated based on the timing uncertainty in the equipment, the spatial resolution of the cameras, and the settling and inertial effects of the suspended particles. The uncertainty from the equipment was calculated to be $\pm 2e\text{-}9$ m/s. The uncertainty due to the spatial resolution of the cameras was ± 0.3141 m/s and was the largest source of uncertainty in the experiment. The uncertainty due to the spatial resolution was calculated assuming a maximum error of 1 pixel for particle location as measured by the CCD, corresponding to a distance of 0.25 mm. The settling uncertainty, based on the settling velocity of the particles, was ± 0.001 m/s. The inertial uncertainty, measuring the uncertainty in the particles following the movement of the fluid, was ± 0.081 m/s. Ideally, the uncertainty would be calculated statistically based on a know value such as free stream velocity. The lack of a known velocity inside the particle box prevented a statistical type uncertainty analysis. The total uncertainty was on the same order as the uncertainty measured in the SAPIV experiments by Belden et al. [16]. The equations used for the PIV uncertainty calculations can be seen in Appendix A.

2.1.2   2DPIV

The same setup for the SAPIV was used for taking 2DPIV measurements. The center camera in the camera array was the only camera used in the 2DPIV experimental runs. A cylindrical lens was attached to the laser to create a thin vertical laser sheet 2 mm in thickness for particle illumination. The same pulse signals from the signal generator were used, providing the same timing as the SAPIV experiments. The laser sheet was positioned parallel to the *xy*-plane at 65% of the half span, or 8 cm from the base of the left wing, as shown in Figure 2.3.

The 2DPIV image pairs were processed using DaVis Imaging Software produced by LaVision. DaVis performed 3 passes on the images pairs, with a final correlation window of 16x16 pixels with 50% overlap. This equated to a 4 x 4 mm^2 (4 pix/mm) window of interogation. This resulted in a total of 16,384 vectors in a vector field of 128 x 128 vectors in the *x* and *y* directions. Vorticity was calculated using a built-in DaVis 8-point circulation method.
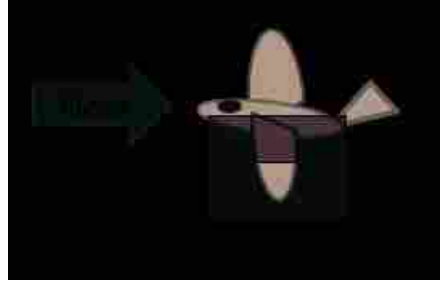
Figure 2.3: The laser sheet for the 2DPIV experiments was 2 mm in thickness and positioned parallel to the *xy*-plane at 65% of the half span, or 8 cm from the base of the left wing.

A higher density of particles was acheived in the 2DPIV experiments. There were a total of 23,616 particles detected with a particle density of 0.0225 ppp. This increased density of particles contributed to the improved spatial resolution of the 2DPIV results. Another reason for the difference in spatial resolution between the 2DPIV and SAPIV results is the trade-off between the *x* and *y* resolution for the *z* depth inherent to the SAPIV technique as described by Belden et al. [16].

The overall uncertainty of the 2DPIV velocity measurements was 0.3141 m/s, or $\pm17\%$ velocity error, as compared to the average velocity. This uncertainty was calculated in a manner similar to the SAPIV uncertainty. The differences in the uncertainty calculations from the SAPIV uncertainty were the timing uncertainty and inertial uncertainty, due to the difference in average velocity. A different average velocity was expected because the SAPIV calculated an average velocity for the entire volume while the 2DPIV only calculated an average velocity for a localized plane. The uncertainty from timing was $\pm$1e-9 m/s. The inertial uncertainty was ±0.050 m/s. The largest sorce of uncertainty was the spatial resolution, ±0.3131 m/s. The equations used for the PIV uncertainty calculations can be seen in Appendix A.

2.2 Force Measurement

Force measurements were acquired using an Interface Model SMT 5.6 lb. load cell. The load cell was connected to a National Instruments cRio chassis. A LabView VI was written to control the load cell and to control the high speed camera used for wing tip position tracking. The VI was burned onto the cRio chassis for faster execution. The load cell aqcuired force measurements at 4000 Hz.

12

Figure 2.4 shows the force data acquired with the load cell. A 150 Hz component in the force data was detected after performing an FFT on the force data signal (Figure 2.4(a)). A closer inspection of the experimental setup revealed that the 150 Hz component of the signal was from vibrations of the motor and mechanical linkage assembly, not from the forces generated by the movement of the wing. Therefore, the 150 Hz signal could be neglected. The load cell data was filtered using a low-pass 100 Hz butterworth filter (Figure 2.4(b)) to remove the 150 Hz signal while retaining all lower frequency signal contributors.

(a)   (b)
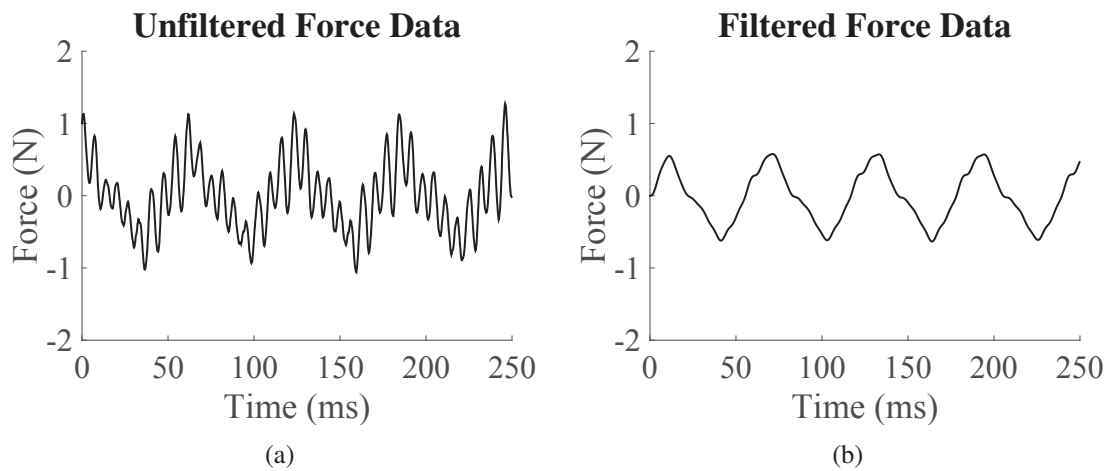
Figure 2.4: Plots of the force data. The force data exhibited a 150 Hz component in the signal, visible in (a). Upon further inspection, the 150 Hz component of the signal was found to be generated by vibrations from the motor and mechanical linkage assembly in the MAV. A low-pass 100 Hz butterworth filter was applied to the signal to remove the 150 Hz vibrations from the signal, show in (b).

A camera was used to track the wing tip of the MAV. The camera shutter was synced with the load cell signal using LabVIEW and captured images at a rate of 2000 Hz. The MAV flaps at 15-17 Hz, making the Nyquist frequency 30-35 Hz. The 2000 Hz shutter speed was chosen to correspond with the available built in camera frame rate of 2000 fps, At this rate, there were, on average 122 images for each flapping period. The 4000 Hz load cell sampling rate was chosen for ease in syncing the load cell sampling with the camera image acquisition. Further explanation of the LabVIEW code and screenshots of the block diagrams are included in Appendix B.

The number of data points and images acquired was limited by amount of memory storage on the camera. At 2000 fps and a resolution of 256 x 768 pixels, a maximum of 7260 frames, or

3.63 seconds, could be recorded. The 7260 frames allowed for an average of 59 flapping cycles per run. The images of the wing tip from the force measurement experiments were used to sync the force measurement experiments with the flow field measurement experiments.

Twenty-one experimental runs were performed. The first ten runs were performed with the MAV in the horizonal position for measuring vertical forces as shown in Figure 2.5(a). A second ten runs were performed with the MAV in the vertical position for measuring horizontal forces as shown in Figure 2.5(b). A final run was performed with the MAV in the horizontal position with a second camera positioned near the first camera. A direct linear transform (DLT) was performed on the images from the two cameras to find the 3-dimensional position of the wing tip to track out of plane motion.

The flapping cycles in each run were phase-locked and were both averaged and ensemble averaged. The average lift force uncertainty was ± 0.0019 N, or $\pm 13.2\%$. The average thrust force uncertainty was ± 0.00079 N, or $\pm 1.0\%$. The larger uncertainty in the lift force was due to an oscillation in the peak lift values from one cycle to the next in each run. The ensemble averaged data uncertainty was on the same order of magnitude, but varied at each point in the flapping cycle.

The wing tip position was tracked using the images from the cameras. A series of preprocessing steps were used to adjust the images to allow for wingtip tracking, as shown in Figure 2.6. All images, including the DLT, were preprocessed using the same algorithm. First, a mask was generated for each set of images from each run (Figure 2.6(a)). An average image for each run was created using all of images from the run. The average image was then thresholded using a threshold value calculated with the Otsu method, that is, a threshold value that minimized the intra-class variance between the two levels of the thresholded image. The averaged image was then dilated using a "disk" element with a radius of 1 pixel. The dilation of the white space features in the thresholded image provided a larger mask for future steps that reduced the chance of nonmoving features in the images being left after masking.

Figure 2.6(b) represents an unprocessed image. Each image in the sequence was thresholded using the calculated threshold value used for the average image (Figure 2.6(c)). Each image was then masked by subtracting the average image from the tracking image (Figure 2.6(d)). The masked image was then eroded with a "disk" element with a 1 pixel radius and dilated with a "disk" element with a 4 pixel radius (Figure 2.6(e)). This step was to first remove any small white spaces,

14

(a)   (b)
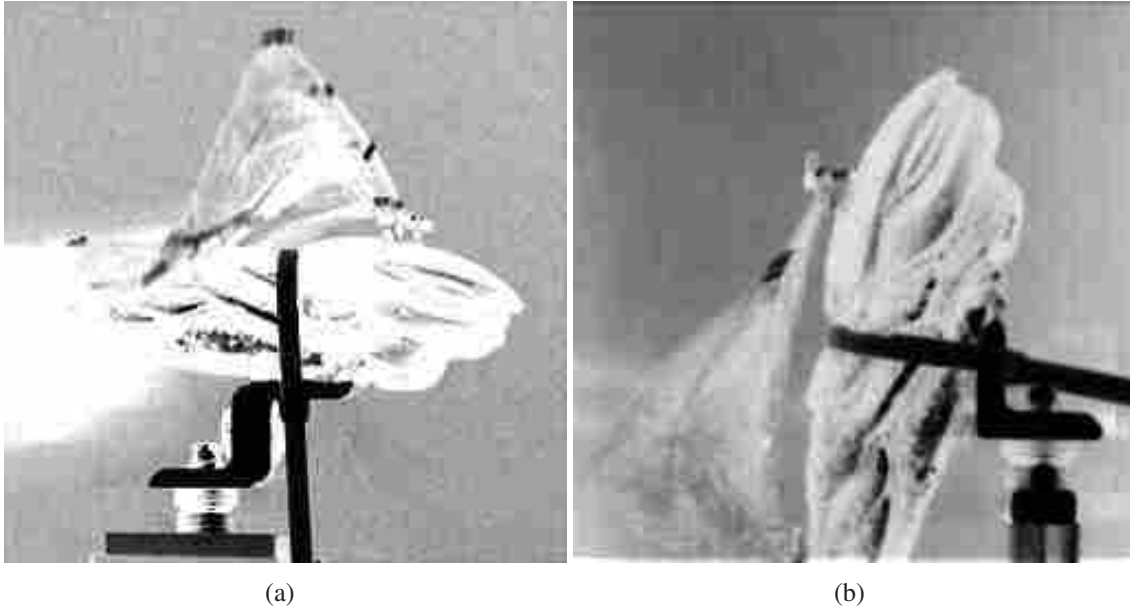
Figure 2.5: 21 experimental runs were performed on the MAV using 2 different positions. 10 runs were performed with the MAV in the horizonal position for measuring vertical forces (a). 10 runs were performed with the MAV in the vertical position for measuring horizontal forces as shown in (b). 1 run was performed with the MAV in the horizontal position with a second camera positioned near the first camera to perform a direct linear transform for 3D information.

then create larger connected components for analysis. The connected components were identified as well as their centroids using a built-in Matlab algorithm. The initial wing tip position was found by manually selecting the connected component associated with the wing tip. Figure 2.6(f) shows the final image with the selected component circled for emphasis. With each successive image, the euclidian distance from each connected component to the previous wing tip position was compared. The connected component with the minimum distance was classified as the wing tip and the centroid was recorded as the wing tip position of that image.

The runs were phase-locked and ensemble averaged. The uncertainty in the x direction was ± 4.46 pix, or $\pm 2.0\%$. The uncertainty in the y direction was ± 8.6 pix, or $\pm 1.7\%$

The wing tip was found to disappear 2 or 3 times out of 7260 images in each run, and in such cases, the previous wing tip position was used as the current wing tip position if the missed point was during the first flapping period (Figure 2.7). If the missed point occured during subsequent flapping periods, the last recorded location at that time in the previous flapping period

(a) (b) (c) (d) (e) (f)
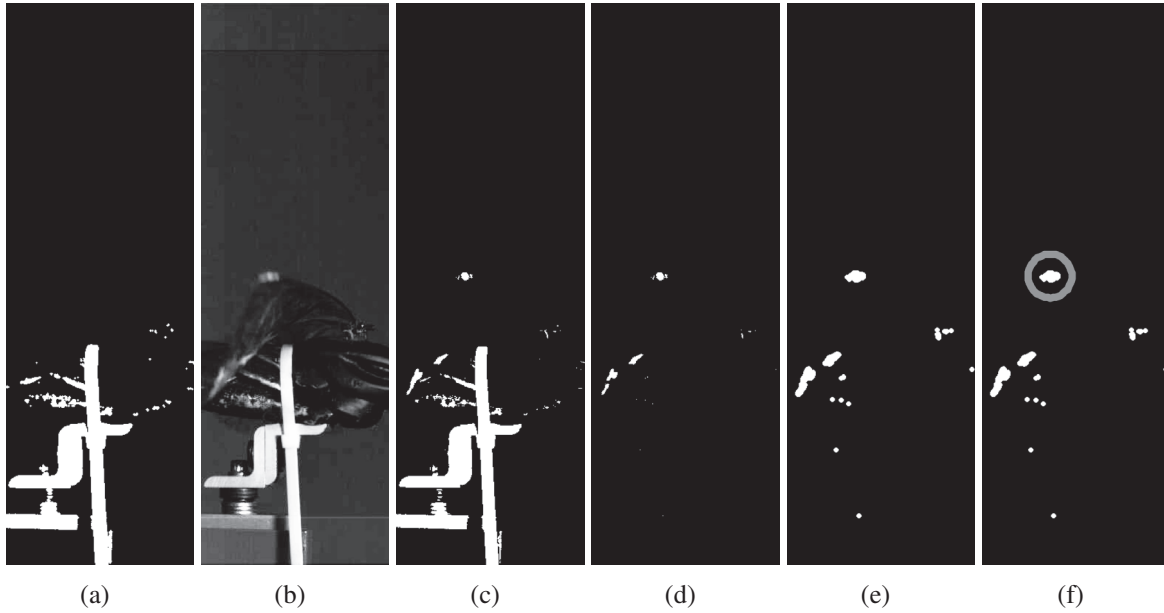
Figure 2.6: A series of prepocessing steps were used to adjust the images to allow for wingtip tracking. A mask was generated for each set of images from each run (a) by averaging all of images from the run, thresholding the image, then dilating image. (b) represents an unprocessed image. Each image in the sequence was thresholded using the calculated threshold value used for the average image (c). Each image was then masked (d). The masked image was eroded and dilated (e). The connected components were identified as well as their centroids using a built-in Matlab algorithm, and the initial wing tip position was found by manually selecting the connected component associated with the wing tip (f).

was used. The current wing tip position was not found those 2 or 3 times per run due to the image preprocessing removing the connected component representing the wing tip in one of the preprocessing steps. A maximum distance was set to prevent the algorithm from selecting another connected component if the wing tip connected component was missing from the image. With the algorithm finding the wing tip in 99.96% of the images, the use of the previous wing tip position was deemed appropriate. This introduced, on average, 2.3% difference in wingtip location if the point were missing in the first flapping period, and a 1.9% difference in wingtip location if the point were missing in subsequent flapping periods. These error levels were on the same order as the uncertainty of ensemble averaged data.

Wing Tip Position
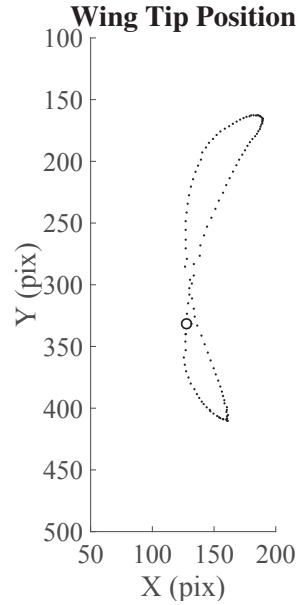
Figure 2.7: The wing tip tracking algorithm identifies the cartesian coordinate of the wing tip through an image sequence. The wing tip is not found in 2 or 3 out of 7260 images in each run, represented by a circle in the figure. The previous wing tip position is used when the wing tip cannot be found.

2.2.1 Direct Linear Transformation

The DLT was performed using the algorithm outlined by Scott Thomson [18]. The goal of a DLT is to transform the pixel locations of an object, in this case the wing tip, in the two images to the cartesian coordinates $[x, y, z]$ in the measurement volume. To perform a DLT, two cameras are directed towards a volume of interest. Calibration points are designated within the volume of interest where the cartesian locations are known. To simplify this step, a calibration target can be used and placed on different planes within the volume of interest so that the x, y, and z locations of the points on the calibration target are easily measured and recorded. An image is captured from each camera with the calibration target on each of the specified planes. The calibration points are identified by pixel location in each image. Using the pixel locations and known cartesian locations of each point, calibration matrices are solved for for the two cameras. The calibration matrices can then be used to estimate the cartesian location of an unknown point by identifying the pixel location of the point in an image from each camera.

7 calibration target locations with 12 calibration points on each plane were used to define the DLT for tracking the MAV wing tip. After performing a preliminary DLT on only one flapping

17

period (122 image pairs), it was found that only 4 calibration targets were needed since the wing tip only traveled through the volume covered by 4 calibration planes. This provided a total of 48 calibration points. The pixel location of the wing tip in each image at each time step was determined using the same algorithm employed for tracking the wing tip in the single camera experiment image sequences (i.e., preprocessing).

Uncertainty was calculated for the x, y, and z measurements for the DLT. The x measurements were ± 0.80 mm, or $\pm 1.23\%$. The y measurements were ± 1.78 mm, or $\pm 11.79\%$. The z measurements were ± 0.79 mm, or $\pm 0.47\%$.

CHAPTER 3.   THREE DIMENSIONAL FLOW MEASUREMENTS ON FLAPPING WINGS USING SYNTHETIC APERTURE PIV[1]

3.1   Abstract

We present the results of 3D velocity measurements of the flow fields around a free flying painted lady butterfly (*Vanessa cardui*) and a tethered mechanical flapper using Synthetic Aperture PIV (SAPIV). The velocity fields presented for the free flying butterfly have limited spatial resolution; however, leading edge vortices (LEV) and trailing edge vortices (TEV) can be seen during the downstroke of the butterfly. The results show that SAPIV has potential as a flow analysis tool to obtain whole-field, time-resolved velocities surrounding freely flying insects. The results of a tethered mechanical flapper focus mainly on the LEV and TEV through an entire flapping cycle. The results are compared to velocity measurements taken using traditional PIV techniques. Additionally, force measurements of the lift and thrust generated by the mechanical flapper are compared with the calculated forces from the measured velocity data and circulation in the flow field. The reconstructed visual hull of the butterfly and mechanical flapper is also discussed.

3.2   Introduction and Background

As unmanned air vehicles (UAVs) have become more prevalent, the size of manmade flying machines has decreased. Emphasis has been placed on flapping wing designs for micro air vehicles (MAVs) as research has shown that challenges arise in lift generation and stability in fixed wing flight as the scale decreases [1]. Alternatively, rotary wings, as stated by Clemons et al. [2], "offer good agility and vertical-take-off-and-landing (VTOL) capability, [but] suffer from wall-proximity effects, are too noisy, and usually are inefficient for low Reynolds number flight." Flapping flight

---

[1]The content of this chapter comes from an article published in *Experiments in Fluids*. Langley, K., Hardester, E., Thomson, S., and Truscott, T., 2014. "Three-dimensional flow measurements on flapping wings using synthetic aperture piv." *Experiments in Fluids*, 55(10). The contributions to the paper by Eric are all of the MAV experiments, results, and analysis.

19

has its own challenges, including recreating the kinematics of a flapping wing, but allows for greater lift generation and stability at small scales and low Reynolds numbers.

In order to better understand small-scale flapping regimes, experiments are used to analyze how natural and man-made fliers generate the appropriate forces to fly. In recent years, particle image velocimetry (PIV) has been employed to characterize flow structures surrounding mechanical models; however, its use in studying flapping flight using living animals has been limited. To date, there have only been PIV studies published on 14 flying animals: 9 birds, 3 bats and 4 insects [19]. Of these, five studies are focused on two insects: a desert locust, *Schistocerca gregaria* [7, 15, 20], and a hawkmoth, *Manduca sexta*, [21, 22] and one study focused on two species of butterfly, *Cynthia cardui* and *Idea leuconoe* [23].

Many of the PIV studies on living insects have been either 2D or stereo PIV (2D-3C, where C stands for component) performed in a single plane. Bomphrey et al. [15] are the first to have performed a 3D-3C PIV study using tomographic PIV to measure the volumetric, time-resolved wake of a tethered desert locust. Tomographic PIV uses 4 cameras at the corners of the volume to obtain 3D whole-field data. A volume of 60 x 80 x 4 mm^3 was used. The results show previously unseen wake deformation and the authors were able to reconstruct the vortices in the wake of the desert locust through phase-averaged wake measurements.

In addition to observing natural fliers, many studies involve mimicking the wings and wing trajectories of birds or insects, including MAVs. Experiments performed in air and oil [8] often focus on the wing surfaces and the near wake, and data can be collected during impulsive starts and after long time periods [9]. Mechanical mechanisms allow for flapping parameters to be adjusted to study the effect of parameter changes on the flow structures and forces associated with flapping flight. Mazaheri and Ebrahimi [24] studied the effect of wing stiffness on the thrust-to-power ratio of flexible wings in hovering and cruising flight by varying the thickness of the chordwise ribs of the wing.

The repeatable flow patterns of mechanical flapping wings also allows for 3-dimensional information through phase-locking. Lu and Shen [14] used an electromechanical model dragonfly wing to perform 3-dimensional analysis of hovering flight. This was accomplished through multiple stereoscopic PIV slices phase-locked along the span of the wing. A more recent study performed by David et al. [25] explores the 3-D volume around a flapping wing in water using

20

tomographic PIV. The tomographic PIV volumes were stitched together through phase-locking to obtain PIV over the entire wing.

Recently, Synthetic Aperture Particle Image Velocimetry (SAPIV) has been developed to measure 3D fluid motion using an array of cameras to image the volume of interest [16]. In SAPIV, an array of high speed cameras is utilized to capture 3D spatial and time-resolved information of seeded fluid volumes. Using the principles of light field imaging, images from each of the cameras are digitally combined and refocused to create a set of images that are in focus at various planes throughout the volume of interest, a focal stack. This method allows for high seeding densities due to the ability to see around partial occlusions and larger illumination volumes than tomographic PIV [16].

This research measures 3D, time-resolved velocity fields around a painted lady butterfly (*Vanessa cardui*) in free flight and an MAV in tethered flight by using Synthetic Aperture Particle Image Velocimetry (SAPIV). Whole-field velocity data enables the identification of flow structures not seen or measured via other methods and provides access to multiple portions of the flow for further study with only having to collect experimental data once. The technique has been effectively utilized in underwater flow fields surrounding fish [26], vortex rings [16] and multiphase flows [27]. Here we attempt to show the same potential in air. While the butterfly experiment is limited in spatial resolution, the velocity and vorticity qualitatively demonstrate the feasibility of using SAPIV to collect data in free flight situations. Alternatively, data collected from the MAV in tethered flight provides a more controlled experimental environment for obtaining higher spatial resolution. The presence of leading edge vortices during the up and down strokes of the MAV is verified through the calculated vorticity and is compared with *in situ* force measurements. Additionally, this research shows the utility of using SAPIV refocusing algorithms to reconstruct and remove the visual hull of an object (butterfly or MAV) that occludes portions of the measurement volume.

3.3   Experimental Methods

Painted lady butterflies were acquired through an online retailer as caterpillars and grown to maturity in the lab. The butterflies had an average wing span of approximately 6 cm and a body length of approximately 2.5 cm.

Measurements were performed on a commercially available MAV - the iFly Vamp (Interactive Toy Concepts LTD) and painted lady butterflies. The iFly Vamp measures 25.4 cm long, has a 30.5 cm wingspan, and is powered by a small electric motor that drives a pivoting mechanism at the front edge of the wings, with the back edge of the wings pinned. A strut forms the leading edge of the wings with the rest of the wings made of a thin, plastic membrane. Steering is accomplished by moving the pinned back edges of the wings up or down, depending on the direction of the turn. The mechanism is controlled wirelessly through a remote. Stability is achieved through a fixed tail section connected to the back of the body (Fig. 3.1), though the MAV only achieves marginal stability during flight.
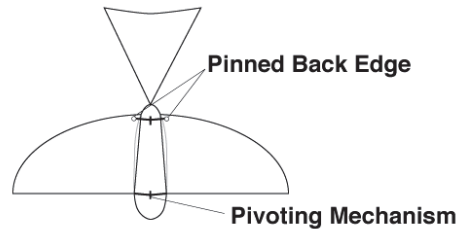
Figure 3.1: A top-view line drawing of the MAV. The MAV is powered by an electric motor that drives a pivoting mechanism at the front edge of the wings, with the back edge of the wings pinned.

3.3.1 Experimental Setup

The butterfly experiments were performed in a custom acrylic observation tank (61 x 41 x 30 cm^3), providing complete optical access. The MAV experiments were performed in a separate acrylic observation tank (60 x 60 x 45 cm^3) to minimize any wall effects from the larger size of the MAV. Data were gathered when a butterfly was placed in the observation tank and allowed to fly freely. In a separate experiment, the MAV was tethered to a steel plate held in place magnetically in the center of the observation tank.

The synthetic aperture setup consisted of 8 Photron SA3 high-speed video cameras at a resolution of 1024 x 1024 pixels. The cameras were equipped with 50 mm lenses and arranged in an array such that every camera was looking at the same region of interest. The camera array was positioned parallel to the long axis of the observation tank as shown in Fig. 3.2.
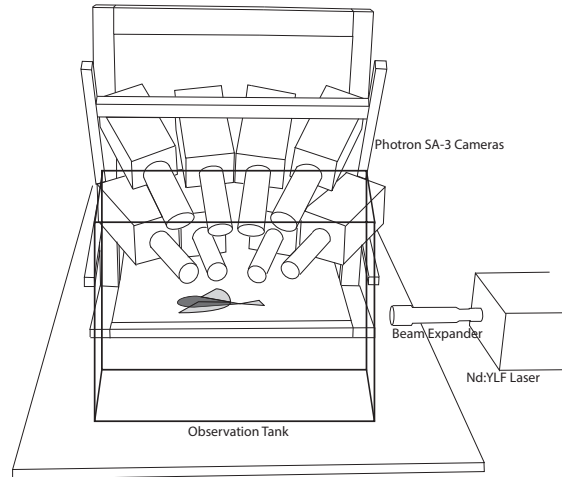
Figure 3.2: Line drawing of the experimental setup. Eight high-speed cameras were used to perform SAPIV. The drawing is not to scale

A Darwin-Duo laser system (Quantronix, Nd:YLF, 1000 Hz) was used to provide PIV illumination. This laser uses two laser pulses at 500 Hz each, corresponding to PIV at 500 Hz. The laser was positioned perpendicular to the cameras. A beam expander (Edmund Optics 532 nm 2-8x 64418) was used to enlarge the beam to a cross sectional area of 55.8 cm^2.

The air inside the tank was seeded with hollow polymer microspheres with a mean diameter of 40 μm and a density of 25 kg/m^3 (Expancel, 461 DET 40 d25). The settling velocity of the particles was 0.001 m/s and the inertial time constant was 5.51 μs (Stokes number based on the average velocity was 0.0051).

3.3.2   Image Preprocessing

The raw images from each camera underwent a preprocessing step prior to SAPIV processing. Preprocessing reduced differences between images due to the laser pulse, removed background noise, and removed the butterfly and MAV wing from the respective PIV images. Figure 3.3 illustrates the preprocessing sequence using an image during the takeoff of the butterfly.

Figure 3.3(a) shows a raw image of the butterfly. Only 8-bits of a 12-bit image were used for processing. The first preprocessing step was to bit-shift the image to use the first 8-bits of the 12-bit image instead of the default last 8-bits in order to increase the brightness of the particles.

Bit-shifting was not required for the MAV images. The image was then cropped around the particle field and thresholded using Otsu's method [28] (see Fig. 3.3(b)). Next, the image was thickened with a 3 x 3 kernel of ones, which increased the size of the objects in the image without connecting previously unconnected components (see Fig. 3.3(c)). The thickening operation was performed to increase the size of the small parts of the butterfly, such as the antennae, that would be lost by performing a regular dilation or erosion. In the thickened image, connected components were found and those larger than 100 pixels were kept. The image was then dilated and eroded 5 times by a 3 x 3 kernel of ones to fill in any gaps or holes in the connected components, shown in Fig. 3.3(d). The connected component image was intersected with the bit-shifted image to retain the grayscale values (Fig. 3.3(e)). The large, grayscale connected components were then subtracted from the bit-shifted image leaving only the particles in the image. The final step was to square the intensity values to reduce background noise.

The following technique employed by Belden et al. [16] was used to equalize the brightness and contrast for each time step after the butterfly or MAV wing was removed (Fig. 3.3(f)). First, a sliding minimum in a 10 pixel window was subtracted across the image. The image was then smoothed with a 3 x 3 Gaussian kernel and the histogram of the image was equalized with the histogram of the image with the highest contrast from the time series. The contrast was further boosted by trimming the upper and lower 0.1% intensity values. The final step was to once again subtract a sliding minimum using a 10 pixel window.

3.3.3 Visual Hull

After the subject (butterfly or MAV) was isolated during preprocessing (Fig. 3.3(e)), the visual hull of the subject could be reconstructed. Adhikari and Longmire [29] define the visual hull as the volume that is occluded from the camera view by an object. In this study the visual hull was reconstructed using multiplicative synthetic aperture refocusing as opposed to the additive refocusing used to reconstruct the particle field. Using the multiplicative refocusing option in the SAPIV software creates a cleaner reconstruction of the object by reducing the ghost images of the object caused by out of focus portions of the object from different focal planes (see Belden et al. [16] for more details on multiplicative algorithm). After the visual hull was reconstructed, it was used as a mask and subtracted from the particle field prior to PIV processing.
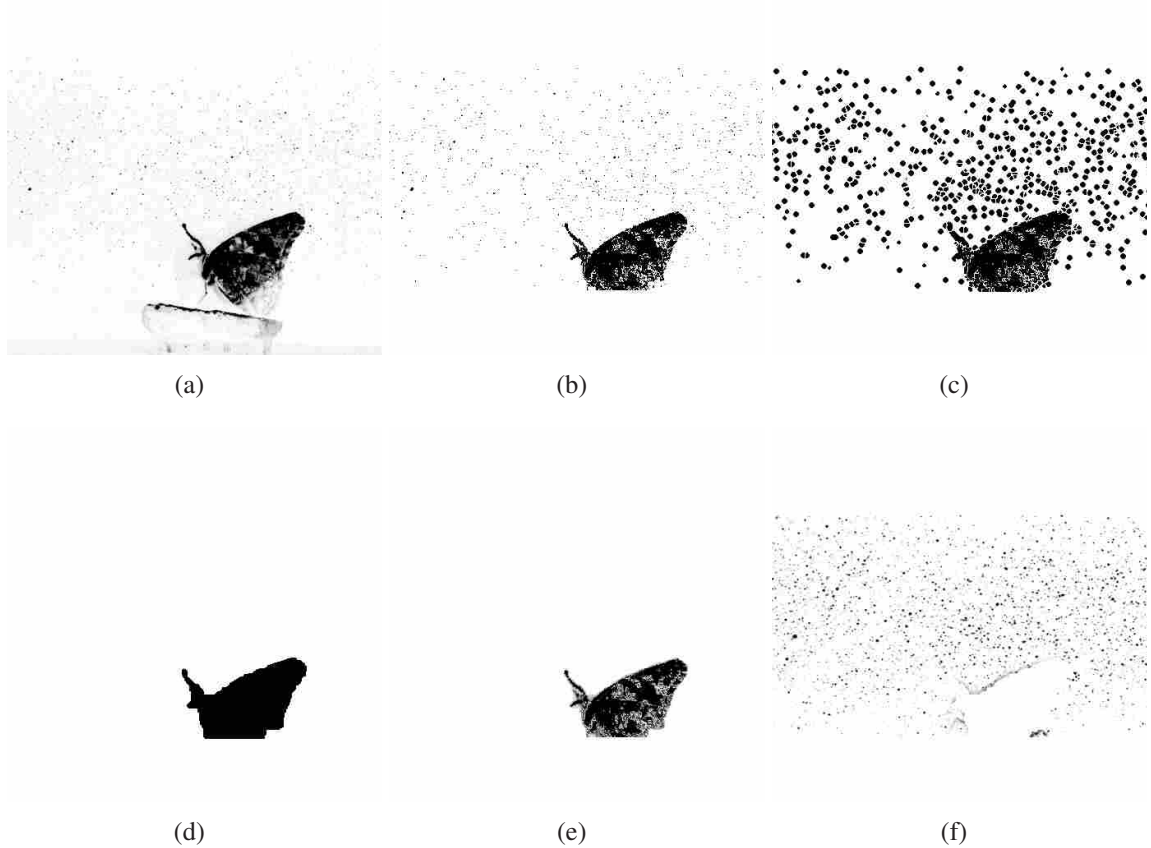
Figure 3.3: Image processing sequence to remove butterfly from images. The raw image is first shown in (a). (a-b) Bit-shifted, thresholded and cropped, (b-c) morphologically thickened, (c-d) dilated and eroded largest connected components 5 times, (d-e) intersection of (d) with (b), (e-f) squared image intensities and equalized intensity histogram for all images. This same process was used to remove the wing of the MAV.

3.3.4 Synthetic Aperture PIV

Three-dimensional, time-resolved fluid velocities were obtained using 3D SAPIV [16]. SAPIV is based on the principles of light-field imaging. The essential idea is that an array of cameras can image an object from multiple view points. Since each viewpoint sees the object from a different angle, the images from each camera can be digitally refocused to create a set of images that are in focus at different planes throughout the region of interest, known as a focal stack. Multiple viewpoints have several advantages such as allowing for high-seeding densities because of the ability to see around partial occlusions. Particles that are in focus on a given plane will have a higher intensity than particles that are not in focus. The out-of-focus particles can be eliminated

from the image planes using thresholding. The digitally refocused and thresholded image pairs can then be passed to a standard 3D PIV system such as matPIV for cross-correlation.

The cameras were calibrated using a process based on the Multi-camera Self Calibration Method developed by Svoboda et al. [30]. A checkerboard calibration target was positioned at several positions in the region of interest. Images were recorded at each position and the corners of the checkerboard grid were found using an auto-correlation method in each image. The image coordinates for each grid intersection, from every plane and camera, were then passed to the self calibration program. Using epipolar geometry, the self calibration calculated a camera projection matrix, which contains both intrinsic and extrinsic camera parameters (i.e., a matrix for each camera containing conversions from image plane coordinates to global coordinates) as outlined in Hartley and Zisserman [31]. This matrix was used in the SAPIV software to correlate objects seen in the various cameras.

The preprocessed images from each of the 8 cameras and the camera projection matrix were passed to the SAPIV software. A map-shift-average algorithm was used to digitally refocus the images onto synthetic focal planes to create a focal stack. For detailed information on how the algorithm works see Belden et al. [16] (algorithms can be obtained at www.saimaging.org).

Velocities were calculated using a multi-pass algorithm with a final interrogation window of 64 x 64 x 32 voxels with 50% overlap in matPIV. This equated to a window size of 16 x 16 x 8 mm^3 (4 pix/mm) for both the butterfly and MAV experiments. This resulted in a total of 1302 vectors in a vector field with 31 x 6 x 7 in the x, y, and z directions, respectively. Vorticity was calculated based on the velocity vectors using an 8 point circulation method [32].

3.3.5 Force Measurements

The lift and thrust forces generated by the flapping wing of the MAV were measured with an Interface SMT S-Type single axis load cell (Interface SMT1-5.6). The MAV was statically mounted in a manner similar to the SAPIV setup. Force measurements were taken for 10 different runs, with 55 flapping periods in each run for statistical analysis. The MAV was mounted in two configurations - horizontally for lift measurements, and vertically for thrust measurements. A single SA3 camera was synchronized with the load cell to document the position of the wings of

the MAV as force data points were acquired. The load cell sampled at 4000 Hz and the camera sampled at 2000 Hz.

3.4 Results and Discussion

3.4.1 Painted Lady Butterfly Results

Velocities were measured during takeoff of a painted lady butterfly. Fifty consecutive image pairs were collected at 1000 fps covering 2.5 wingbeats. Bimbard et al. [33] showed that one wingbeat was not sufficient for takeoff of *pierid* butterflies and that butterfly legs generated the largest portion of the takeoff force. They also showed that the primary direction of the butterfly at takeoff is governed by the force and motion of the legs. In our experiment, we were not able to measure the takeoff force. However, we noticed that takeoff of the butterfly occurred after the first downstroke, lifting it off of the perch and into the laser beam. During the next downstroke the butterfly turned toward the camera and began diving to leave the laser beam thus losing lift. The wingbeat frequency was 25 Hz for the images gathered corresponding to a Reynolds number based on the wingtip velocity and mean chord length $(Re = U_t \bar{c}/\nu)$ of approximately 5000. Figure 3.4 shows the raw PIV images from all 8 cameras during one instant in time of the butterfly flight.

Results from the reconstruction of the visual hull are first discussed followed by the SAPIV results. Several time steps during the first downstroke and the first upstroke during the flight studied are presented. Sequential time steps during the second downstroke are also presented.

Visual Hull

Figure 3.5(a) shows an isometric view of the visual hull of the butterfly formed by multiplicatively refocusing images containing only the butterfly (see Fig. 3.3(e)) from each of the 8 cameras. The visual hull is shown as an iso surface marking the edges of the butterfly. Figure 3.5(b) and 3.5(c) show orthogonal views of the visual hull iso surface from the front and side of the volume.

Since the visual hull is simply the volume that is being occluded from the cameras, it does not form a perfect reconstruction of the butterfly. When viewed from the front, as in Fig. 3.5(b),

27
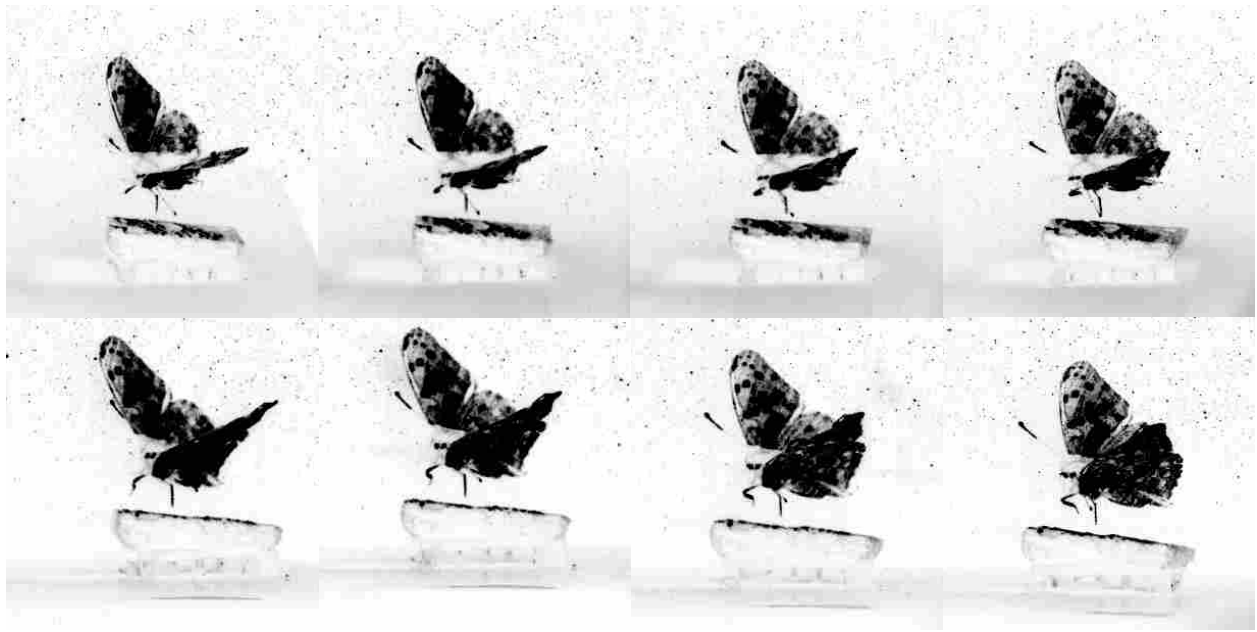
Figure 3.4: Cropped view of the butterfly in flight from all 8 cameras during one instant in time (t = 49 ms).

the butterfly appears as it does in the raw images. The reconstruction is even able to capture the curve of the wings during the upstroke. When viewed from the side (Fig. 3.5(c)), it is clear that the volume behind the front edge of the wings is not reconstructed nearly as well. Instead of the reconstruction following the slope of the wing, it continues at nearly the same level as the front edge. Although this is an imperfect reconstruction, it is able to mark the portions of the volume which cannot be seen and thus it is the volume in which no velocities can be measured. For this reason the visual hull is used as a mask and subtracted from the reconstructed particle field prior to calculating the PIV cross-correlations.

SAPIV Results

Figure 3.6 shows iso surfaces of vorticity about the z-axis for 12 time steps from a single flight covering 1.25 wingbeats. The butterfly is in a downstroke from 1 ms to 19 ms. The upstroke begins at 25 ms and persists until 43 ms. The first half of the subsequent downstroke is then shown (45 - 51 ms). In each vorticity plot, an image of a butterfly has been positioned representing the actual wing position of the butterfly during flight as indicated by the visual hull and PIV images.

28
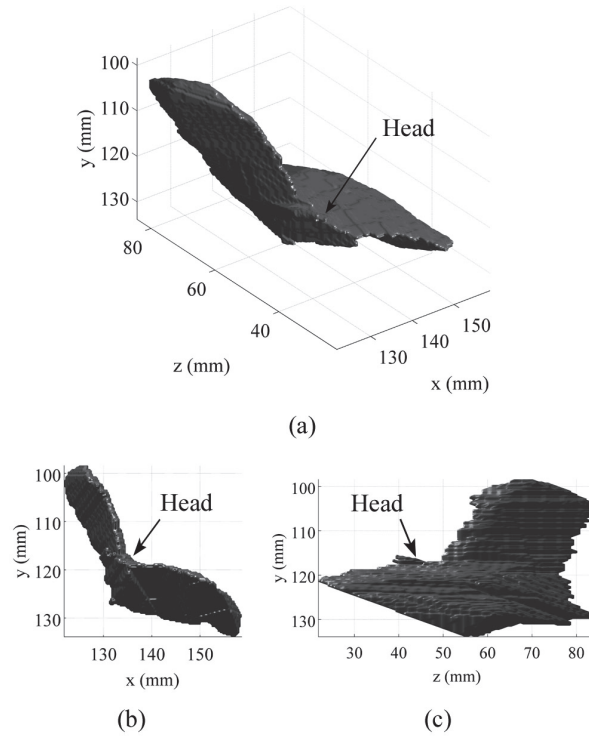
Figure 3.5: Visual hull of butterfly created by multiplicatively refocusing images containing only the butterfly at t = 74 ms. (a) Isometric view (b) frontal view of visual hull (c) projection on to y-z plane. Notice the degradation in reconstruction quality in parts that are occluded from the frontal view.

Further clarification of the flow dynamics shown in Fig. 3.6 can be seen in Fig. 3.7 for select times. Figure 3.7 shows 2D slices of vorticity about the z-axis from the 3D data collected for times 7, 19, 47 and 49 ms. These times were selected since the vorticity data at these times is the most interesting of this data set. In this figure, velocity vectors are shown on contours of vorticity.

As seen in Fig. 3.6, as the downstroke progresses from 1 ms to 7 ms, vortices are generated by the separation and plunging motion of the wings. An LEV can be seen in the plot as a counterclockwise rotating vortex (shown in red, see also Fig. 3.7). The LEV is slightly obscured from view by the clockwise rotating TEV (blue). These vortices are more clearly seen later in the downstroke at 19 ms. At this time, the vortices are much more distinct as the butterfly nears the end of the downstroke. It should be noted that the large vortices seen at times 7 ms and 19 ms are not seen at 13 ms. The vortices should be seen at this intermediate time, however, due to image noise or the coarse resolution of the vector field, only small portions of the vortices are seen.
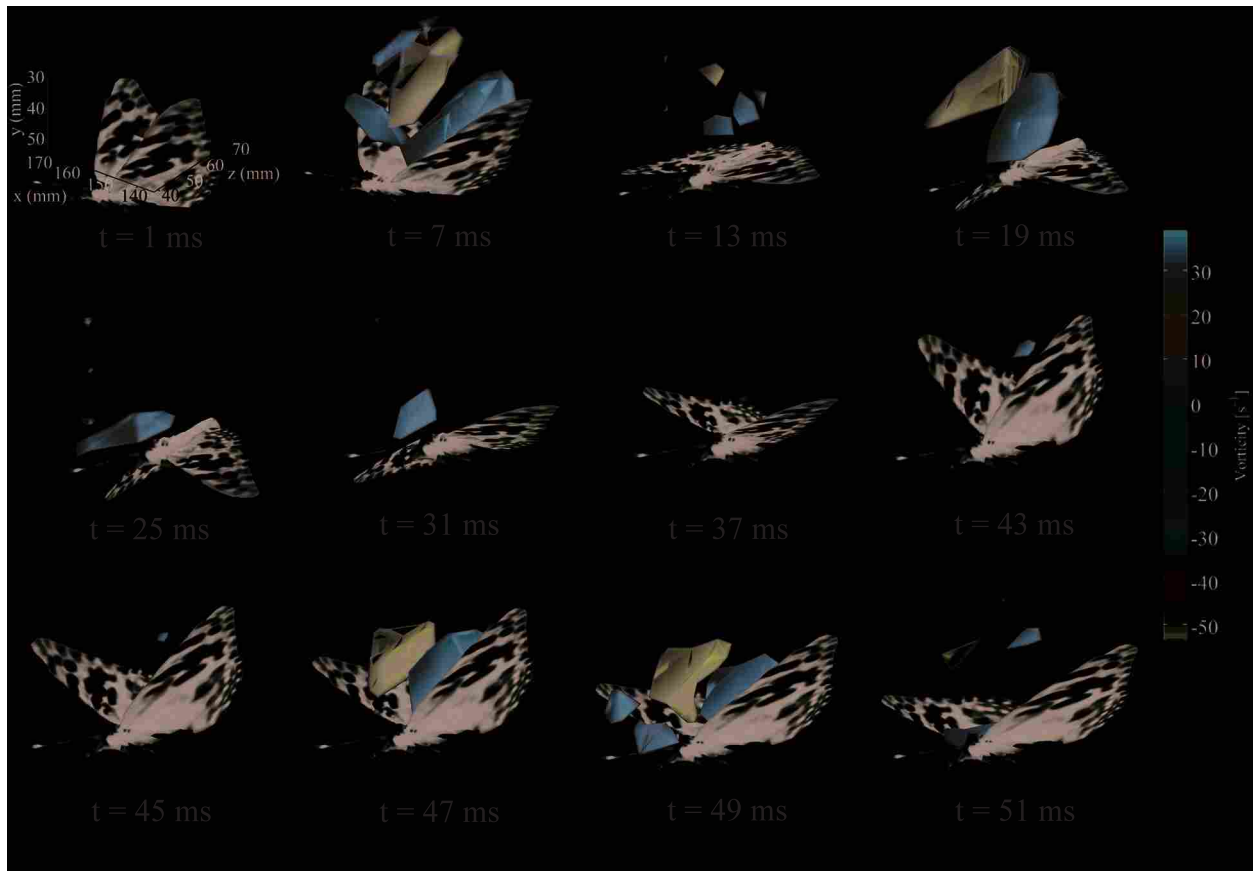
Figure 3.6: Iso surfaces of vorticity about the *z*-axis plotted for 12 time steps covering 1.25 wing-beats. A downstroke persists from 1 ms to 19 ms. An upstroke is shown from 25 ms to 43 ms, and the first half of a downstroke is shown from 45 ms to 51 ms.

As the upstroke begins (t = 25 ms), a portion of the LEV from the downstroke is still visible near the leading edge of the wing. As the upstroke continues through 43 ms, vortices should be generated on the underside of the wing as seen by Fuchiwaki et al. [23]; however, the underside of the wing is outside the measurement volume in this experiment.

As the subsequent downstroke commences, vortices are again generated and are visible at 47 ms. There is a noticeable LEV and TEV near the wing tips. These vortices persist through 49 ms but are no longer visible at 51 ms.

Figure 3.8 presents 3D iso surfaces of vorticity magnitude (35 s^{-1}) at 19 ms and 47 ms showing vortex rings consistent with the pattern diagrams from Fuchiwaki et al. [23]. Traces of these rings are seen in other time steps but are most pronounced in the two time steps presented.
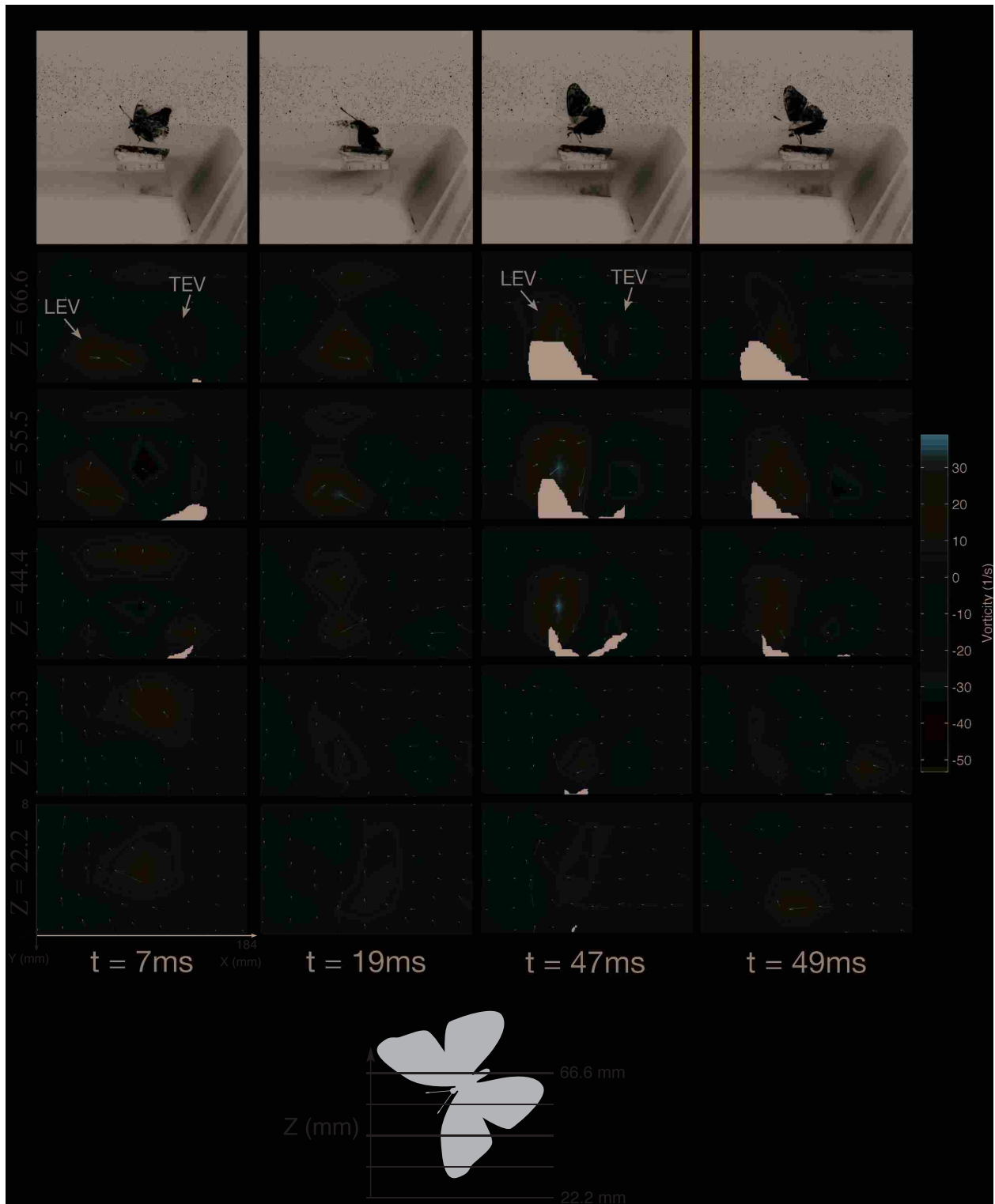
Figure 3.7: 2D PIV slices taken from 3D data shown in Fig. 3.6, velocity vectors shown on contours of vorticity about the *z*-axis. The *z*-axis planes are spaced 11.1 mm apart.
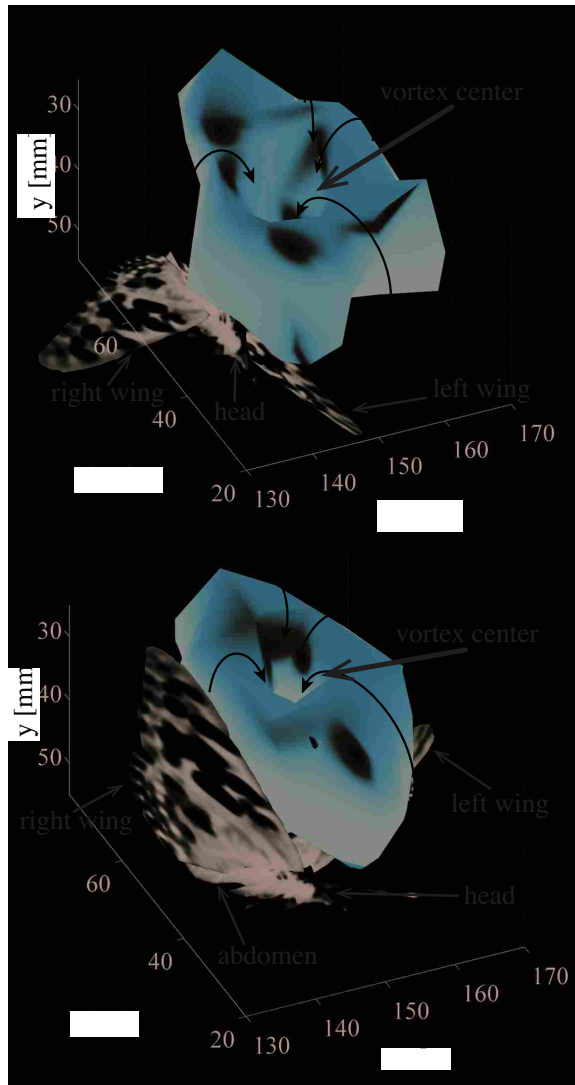
Figure 3.8: Iso surfaces of vorticity magnitude (35 s^{-1}) reveal vortex rings similar to those presented in the pattern diagrams of Fuchiwaki et al. [23].

Discussion

Although the velocity and vorticity results from this study are preliminary in nature and do not reveal any new features in the flow around a butterfly in flight, they show the potential for using SAPIV to obtain 3D, time-resolved, velocities in similarly complex experiments. The results obtained and presented confirm the findings of Fuchiwaki et al. [23], which is the only other published study quantitatively measuring velocities around live butterflies using PIV. The results are also similar to other studies that have made qualitative measurements around butterflies in free

flight (e.g., Srygley and Thomas [34]). The results furthermore highlight portions of the experiment that can be readily improved to obtain better and more quantitatively meaningful results.

The major drawback of the results obtained in this study is the resolution of the vector fields. The fairly sparse seeding and large spatial region of interest resulted in a smallest interrogation volume of 64 x 64 x 32 voxels (16 x 16 x 8 mm^3) resulting in a vector resolution of 8 mm in the x and y dimensions and 11 mm in the z direction, which was insufficient to fully resolve the finer details of the flow structures that are present on the wings during flight. In contrast, the interrogation window used by Bomphrey et al. [15] had a resolution of 2.28 mm in each dimension. This low resolution is not a drawback of the SAPIV technique, but is attributable to drawbacks of the actual experimental setup. To improve on the resolution of the vector fields, large magnification lenses should be used to zoom in closer to the butterfly and the quiescent air should be seeded with a higher density of particles. SAPIV can reliably handle spatial volumes of 50 x 50 x 50 mm^3 with seeding densities up to 0.09 particles per pixel [16].

The visual hull of the butterfly represents the volume in which the butterfly is contained, but it is not a perfect reconstruction of the butterfly. The reconstruction of the visual hull would be vastly improved by having cameras at larger angles surrounding the butterfly than used in this study. A new camera arrangement for future research efforts using 4 cameras on each side of the interrogation volume should improve the reconstruction quality with increasing z-depth spacing.

One advantage of using SAPIV, over 2D PIV or stereo PIV, to obtain whole-field measurements is the ability to analyze the flow structures regardless of the orientation of the butterfly. In the results presented in Fig. 3.6, the butterfly starts with its body parallel to the x-axis but as the flight progressed the butterfly turned, thus, was no longer aligned within the coordinate frame of the reconstructed volume. By looking at the velocity and vorticity components in all directions the vortices on the wings can still be seen.

SAPIV is able to reconstruct 3D whole-field velocity fields in large spatial regions of interest, particularly with large depth of the measurement volume. The depth of the measurement volume possible in SAPIV is greater than that published using tomographic PIV [16]. The largest depth seen in literature by tomographic PIV is 20 mm [35], which may be due to limits in laser optics versus the method; however, the theoretical limits of tomographic PIV have not been addressed in literature to date. While there are other 3D methods that can achieve deep volumes

(e.g., defocusing DPIV and particle tracking velocimetry), the added ability to see around partial occlusions using SAPIV provides a notable advantage.

Uncertainty of PIV Measurements. The overall uncertainty of the PIV velocity measurements is 0.0761 m/s, which corresponds to an uncertainty of 2.38 s^{-1} in the calculated vorticity using the 8 point circulation method [32]. This was calculated based on the jitter in the laser and timing equipment, the spatial resolution of the cameras and the settling and inertial effects of the suspended particles. The largest source of uncertainty is due to the spatial resolution of the cameras. Each pixel of the sensor corresponded to only 0.25 mm in the volume of interest.

3.4.2 MAV Results

Velocities were measured during a start-up flapping period and during cruising flight flapping periods. 597 consecutive image pairs were collected at 250 Hz covering 37 wingbeats. The MAV began flapping with a downstroke motion. The wingbeat frequency was 15.87 Hz, corresponding to a Reynolds number ($Re = 9600$) calculated using the induced forward velocity (1.8m/s) and mean chord length and a Strouhal number ($St = \frac{fL}{V}$) of 0.79 where L is the peak-to-peak amplitude (0.09m), f is the wing beat frequency, and V is the induced forward velocity. It is worth noting that the toy flies poorly, a result of the large Strouhal number being well outside the range of efficient propulsion ($0.2 < St < 0.4$) [36]. The results are given in two sections - the 3D SAPIV results and a comparison between 2D PIV measurements from the MAV and the 3D SAPIV results.

3D Results

Figure 3.9 shows the wing of the MAV through the last 75% of the downstroke in the first six time steps (8-28 ms) and the first 75% of the upstroke in the last six time steps (32-52 ms) with the vorticity about the z-axis plotted as iso surfaces. Images of the MAV that are synchronized with the SAPIV data have been overlaid with the vorticity data from the corresponding time step where the visual hull places the butterfly (to improve visual understanding). Immediately upon

34
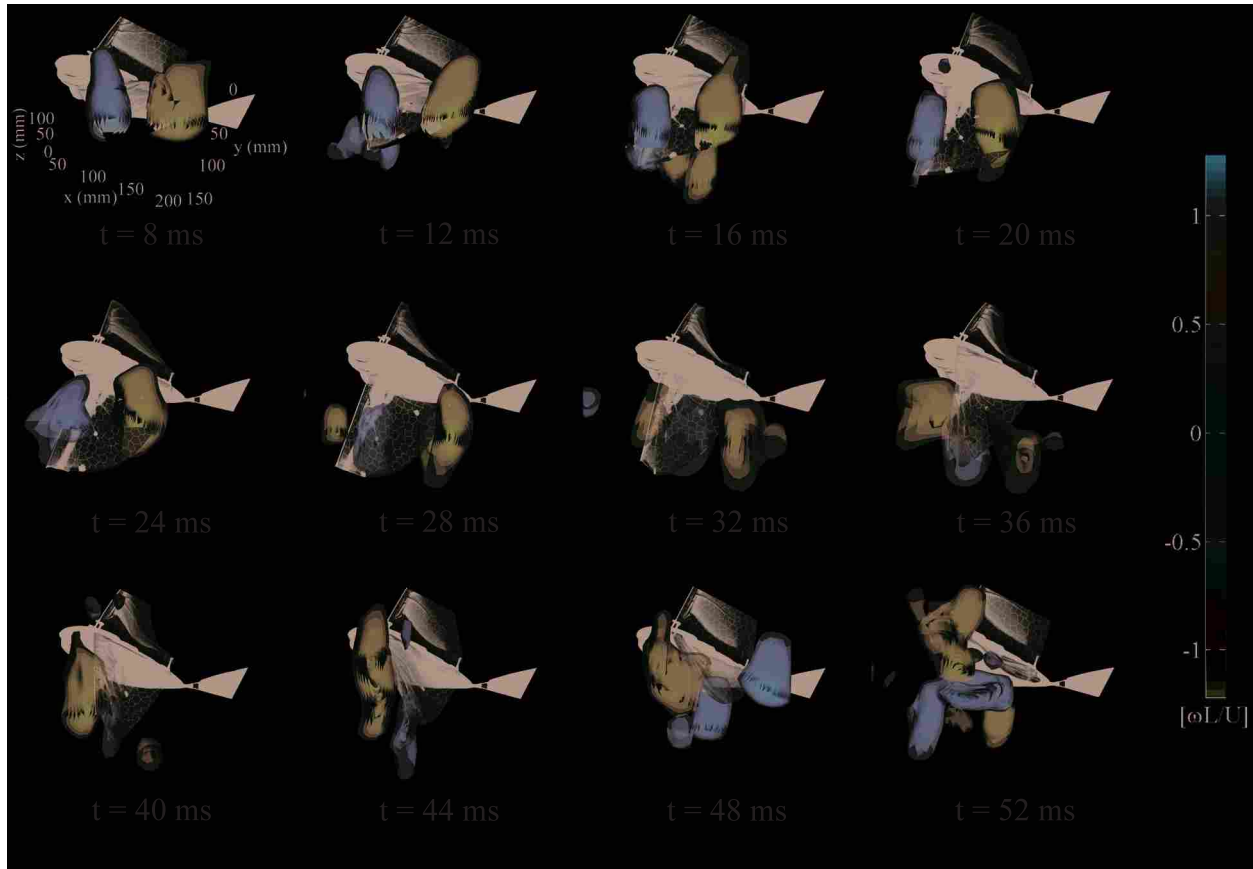
Figure 3.9: Iso surfaces of vorticity about the *z*-axis plotted for 12 time steps covering .75 wing-beats. Times 8 ms to 28 ms show a portion of the downstroke. The upstroke begins at 32 ms and is shown through 52 ms.

inspection, the presence of an LEV and a TEV are recognized on the leading edge (left side) and trailing edge (right side) of the wing, respectively.

The LEV and TEV remain attached to the wing through the entire downstroke and upstroke. The vortices are shed into the wake during the transitions between the up and down strokes. This transition is evident at time = 32 ms. The LEV from the downstroke on the top side of the wing (center structure) is seen leaving the leading edge and moving into the wake as a new LEV (left structure) is seen forming on the leading edge on the bottom side of the wing.

During the downstroke, the LEV and TEV form and remain attached to the top of the wing, and likewise during the upstroke, the LEV and TEV form and remain attached to the bottom of the wing.

A top view of the wing shows the varying shape of the LEVs and TEVs along the span of the wing (Fig. 3.10). A look at the cross section shows that, at the edge of the wing closest to the body, the LEV has a minimum diameter and a maximum diameter closer to the wing tip.

Figure 3.10: Top view of the wing at mid-downstroke. The diameter of the LEV (left) and TEV (right) vary from the edge of the wing closest to the body (top) to the wing tip (bottom). Between the vortices, the visual hull of the wing is shown (black).
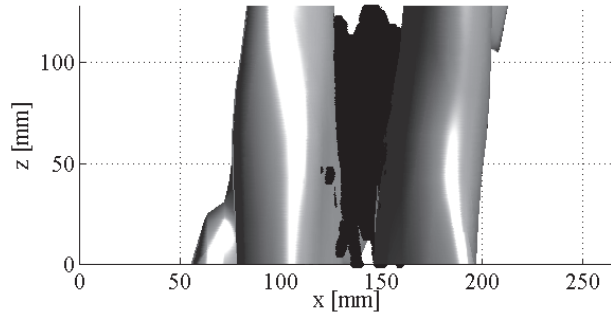
Figure 3.11 shows slices of z-velocities on planes parallel to the xy-plane at time steps 8 ms, 24 ms, and 36 ms. At 8 ms, the wing is near the top of the volume (Y = 0 mm), and high magnitudes of z-direction velocity are observed above and below the wing's location. At 24 ms, the wing is now near the bottom of the volume (Y = 200 mm), and the high magnitudes of z-direction velocity are now observed near the bottom of the volume. At 36 ms, there are three larger sections of z-direction velocities; two negative sections, and one positve. This correlates well with the two large negative vortical structures and one positve vortical structure observed at 36 ms in Figure 3.9, providing evidence of spanwise flow within the LEV and TEV.

2D Comparison

Figure 3.12 shows 2D vorticity slices from the 3D velocity fields at 65% of the half span and the 2D vorticity plots from the 2D PIV at 60% half-span at 14 time steps from mid-downstroke through an entire flapping period (8 ms - 60 ms). The comparison is promising, showing agreement in the formation and behavior of the LEV and TEV on the MAV wing. In both cases, we see the LEV remaining attached to the leading edge of the wing throughout the downstroke. The growth of the LEV can also be seen through the four time steps shown of the downstroke. At t = 20 ms, the
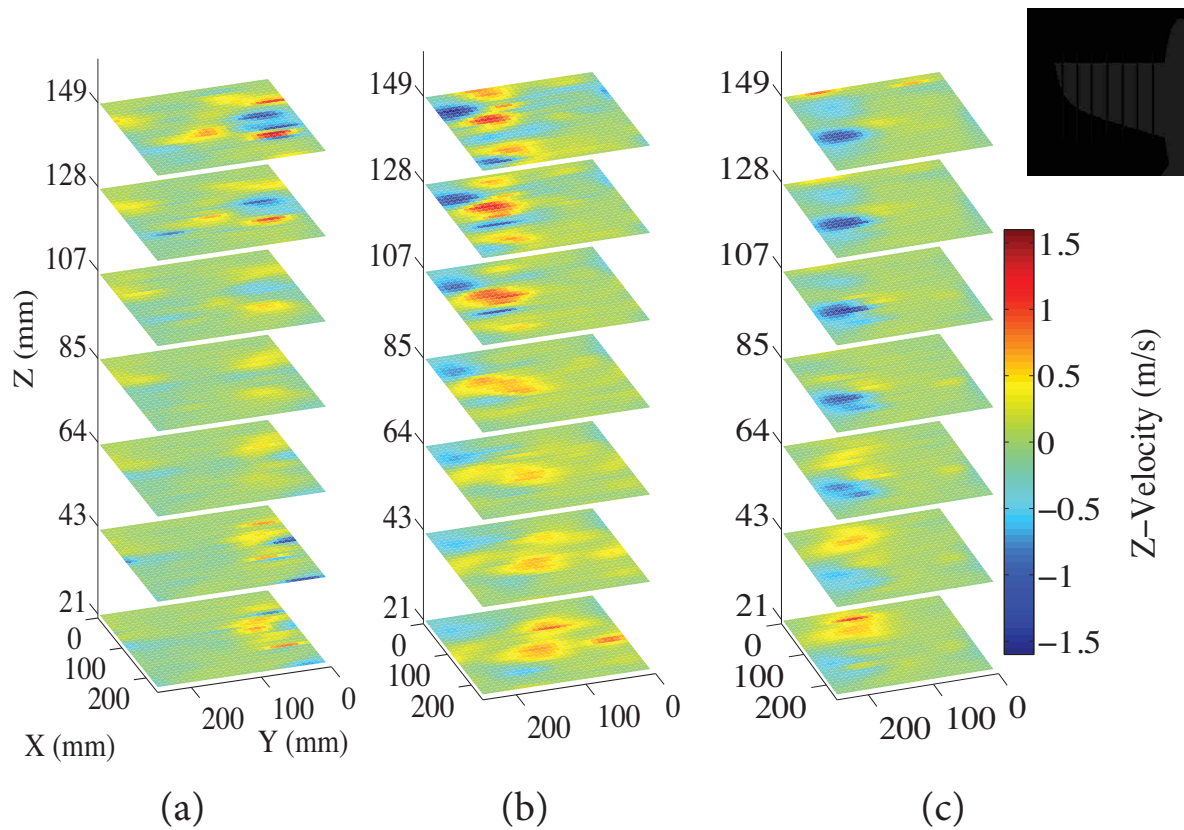
Figure 3.11: Z-direction velocity magnitude plots on xy-planes in the volume of interest taken along the wing as illustrated in the top right corner and where z = 0 mm is at the wing tip. The velocity magnitudes are shown at 8 ms (a), 24 ms (b), 36 ms (c). Positive and negative z-velocites can be seen in (a) at the top of the volume (Y=0mm) within the bounds of the LEV and TEV. In (b), the majority of the z-velocity groupings have moved towards the bottom of the volume (Y=200mm), where the LEV and TEV are located at t = 24 ms. In (c), three larger sections of z-direction velocities are present - two negative and one positive - which correspond to the two negative vorticies and one positive vortex present in t = 36 ms.

wing enters the transition between downstroke and upstroke. The shedding of the TEV is visible and the beginning of the shedding of the LEV is also visible. Ol et al. [37] observed similar vortex structures and shedding patterns around airfoils with sinusoidal pitching and plunging motions in water.

One difference between the SAPIV slices and the 2D PIV is the presence of vortices under the wing in the 2D PIV plots not seen in the SAPIV slices during the downstroke. This is due to difficulty in getting the wings of the MAV to begin in the same location during each run. In the

Figure 3.12: A comparison of the SAPIV (first and third columns) and 2DPIV (second and fourth columns) data with the flapping period shown in 14 time steps. The 3D PIV shows 2D vorticity slices from 3D velocity fields at 65% of the half span as shown in the schematic (upper left).
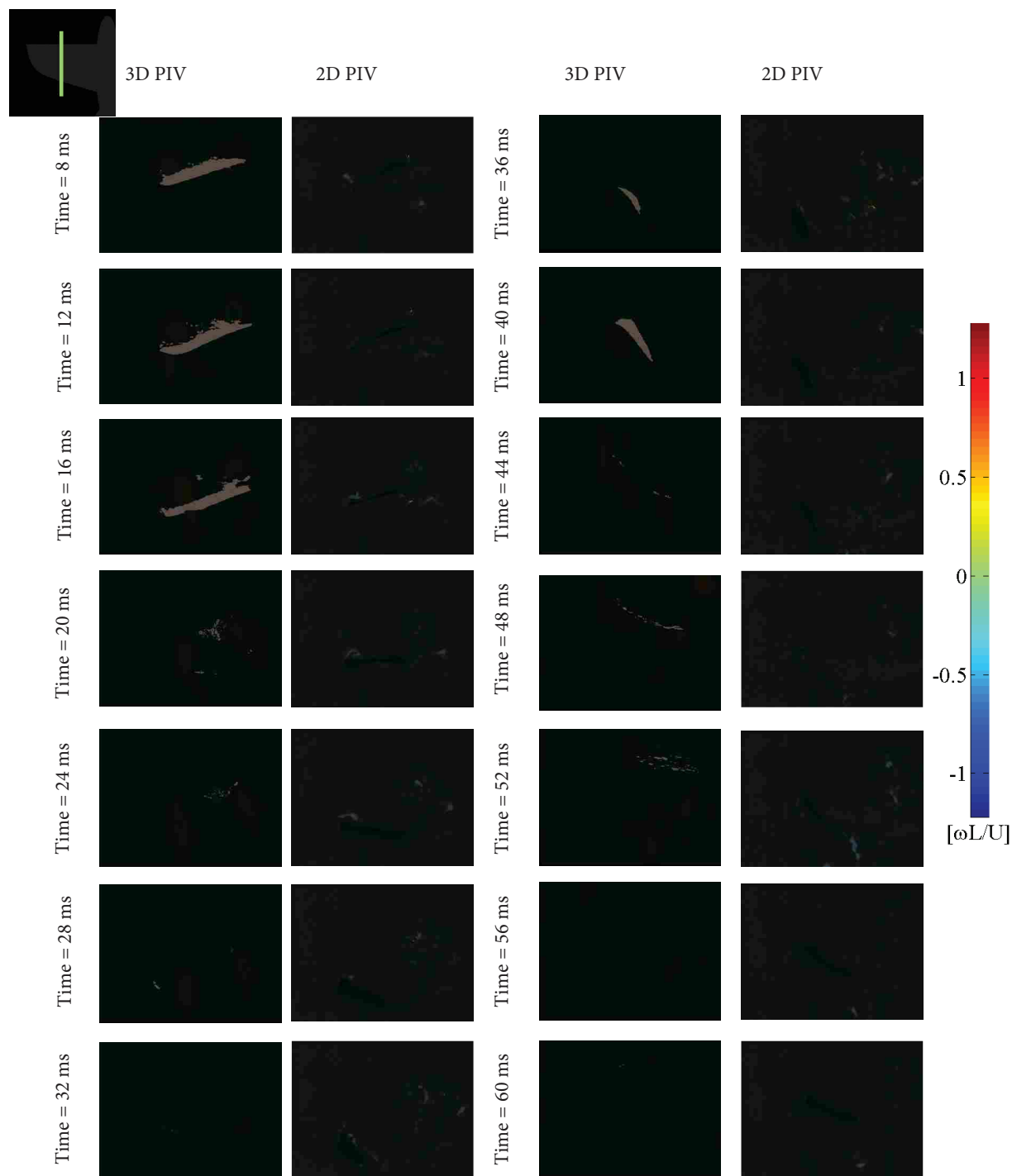
2D PIV run, the wing begins 1/5 of a flapping period earlier than the SAPIV run, allowing enough travel to generate an LEV and TEV in the time before the SAPIV run begins.

Another difference is the fading of the LEV, TEV, and wing in the last three time steps of the SAPIV slices. This is due to the current lower resolution of the SAPIV. The LEV, TEV, and wing are lost in the turbulent flow around the wing in the viewing volume of the SAPIV, while the higher resolution of the 2D PIV allows tracking of the LEV and TEV within the turbulent flow through the end of the flapping period.

Discussion

The visual hull of the wing represents the volume in which the wing is contained, but requires large connected components for the algorithm to process. The reconstruction of the wing could be improved by less particle seeding or by adding more light sources so that the intensity of the wing is the same in all camera views to assist in connected component identification.

As noted in the discussion of the butterfly results, an advantage of using SAPIV to obtain whole-field measurements is the ability to analyze the flow structures regardless of orientation. In the results presented in Figure 3.9, the MAV starts with its wing at an angle of about $45°$ to the Z-axis but as the flight progresses the wing reaches an angle of about $−45°$ with respect to the z-axis . By using multiple cameras, particles that are obscured in one camera view are visible in other camera views, thus providing whole-field measurements at each wing position.

The 2D PIV vorticity plots show greater detail in the LEV and TEV. Despite the lower resolution in the 3D SAPIV data, it is possible to see similarities in the structure and behavior of the vortices. Greater resolution for the SAPIV results could be attained by reducing the size of the volume of interest. However, the reduced size would prevent imaging the entire flapping period in one experimental run when the flapping amplitude exceeds the volume of interest, thus requiring phase locking to combine volumes similar to Bomphrey et al. [15].

3.4.3 MAV Wing Tracking and Force Analysis

Wing Tracking

Initially, the wing position was determined by tracking the wing tip of the MAV and plotting the pixel locations using a single SA3 camera. This resulted in a 2D projection of the location of the wing tip on the plane of the camera sensor. It was observed that the MAV has a skewed figure-eight trajectory, with the figure-eight skewed in the forward direction, in the XY plane (Fig. 3.13(a)) despite being driven by an electric motor through a four-bar linkage, providing only an up and down motion.

A further investigation of the wing tip trajectory was performed by including a second SA3 camera in the acquisition loop and performing a direct linear transform (DLT) analysis of the wing tip position. The trajectory of the wing tip in the XY, XZ, and YZ planes can be seen in Fig. 3.13. The skewed figure-eight trajectory is seen in the XY plane (Fig. 3.13(a)), and the wing trajectory has a curvature with a radius equal to the span-wise length of the wing (Fig. 3.13(c)). The trajectory in the XZ plane (Fig. 3.13(b)) appears to deviate from the symmetric trajectory pattern as in the other planes; however, it can be seen in Fig. 3.13(c) that the wing is not flapping symmetrically with the XYZ axes chosen for the DLT. However, the same symmetry is exhibited along an axis skewed from the chosen XYZ axes.

Force Measurements

Circulation was calculated using the technique described by Epps and Techet [38] where $\Gamma = \sum_{ij} \omega_{ij} \delta A$. A plane at 50% the length of the wing was selected for the circulation calcutions. The circulation was calculated for positive and negative vorticity magnitudes with 25%, 35%, and 50% of the maximum value of vorticity as cut-offs. The circulation over the flapping period is shown in Fig. 3.14. As the cut-off percentage is increased, the magnitude of the circulation decreases, but the shape of the plots remains similar. The 35% of maximum vorticity line was selected for comparison with the measured forces in Fig. 3.15 to correspond with the percentage of maximum vorticity used for visualization of the LEV and TEV in Fig. 3.9, which was 35%.

Figure 3.15 shows the ensemble-averaged lift and thrust forces generated from 55 flapping periods as well as the positive and negative circulation, Γ, calculated using the SAPIV results. The
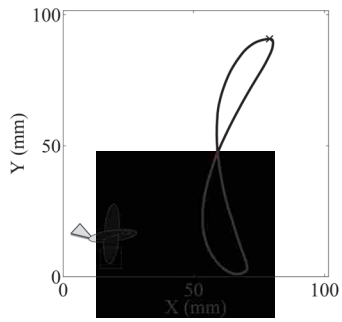
(a)
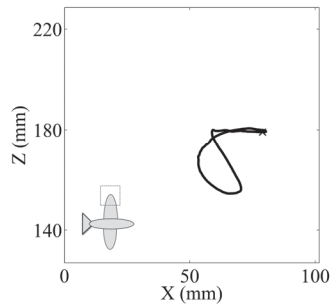
(b)

(c)

(d)

Figure 3.13: 3-dimensional trajectory of the wing tip as determined by performing a DLT analysis. The trajectory is plotted on the *XY* (a), *XZ* (b), and *YZ* (c) planes, as well as an isometric view (d).
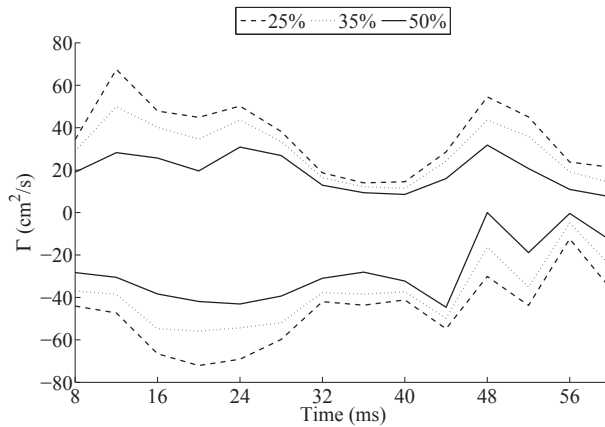
Figure 3.14: The positive and negative circulation plotted at 25%, 35%, and 50% of the maximum vorticity magnitude. Each increase in cut-off percentage shows a decrease in circulation magnitude, but the shape of the plots remain similar.

force data was processed using a 3rd order, 120 Hz low-pass Butterworth filter to remove a 150 Hz signal present in both t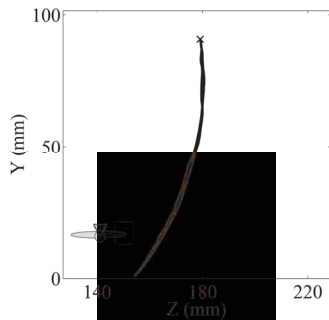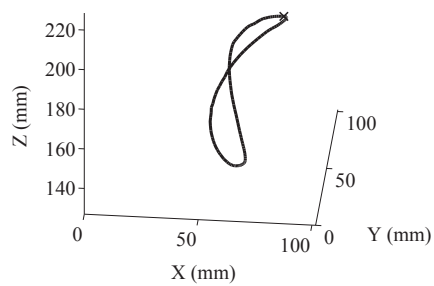he lift and thrust force measurements generated by the motor and gearing of the four-bar linkage driving the wings. The plot is split down the center to distinguish the upstroke from the downstroke of the flapping period. The lift force is represented with the inertial forces removed, calculated using the wing tip tracking data.

In the upstroke, the lift force is negative, with a minimum near the end of the upstroke occurring at -0.579 N. A source of the negative lift force is the downward force generated by the upward movement of the wing. Negative lift can also be attributed to the LEV witnessed on the underside of the wing during the upstroke (Fig. 3.9, 32 ms to 44 ms, and Fig. 3.12, 32 ms to 44 ms). During the downstroke, the forces are reversed; an upward force is generated by the downward movement of the wing, and positive lift is generated. The maximum lift force occurs during the second half of the downstroke at 0.641 N. The lift is generated by the LEV present on top of the wing during the downstroke (Fig. 3.9, 8 ms - 28 ms and Fig. 3.12, 8 ms - 28 ms).

A correlation can be seen between the measured lift force and the calculated circulation in Figure 3.15. As the positive circulation peaks at t/T = 0.4 and 0.73, there are corresponding peaks in the measured lift force, observed at t/T = 0.34 and 0.7, respectively. As the negative circulation peaks at t/T = 0.2 and 0.87, there are corresponding valleys in the measured lift force, observed at t/T = 0.11 and 0.88. The peak and valley in positive and negative circulation can be
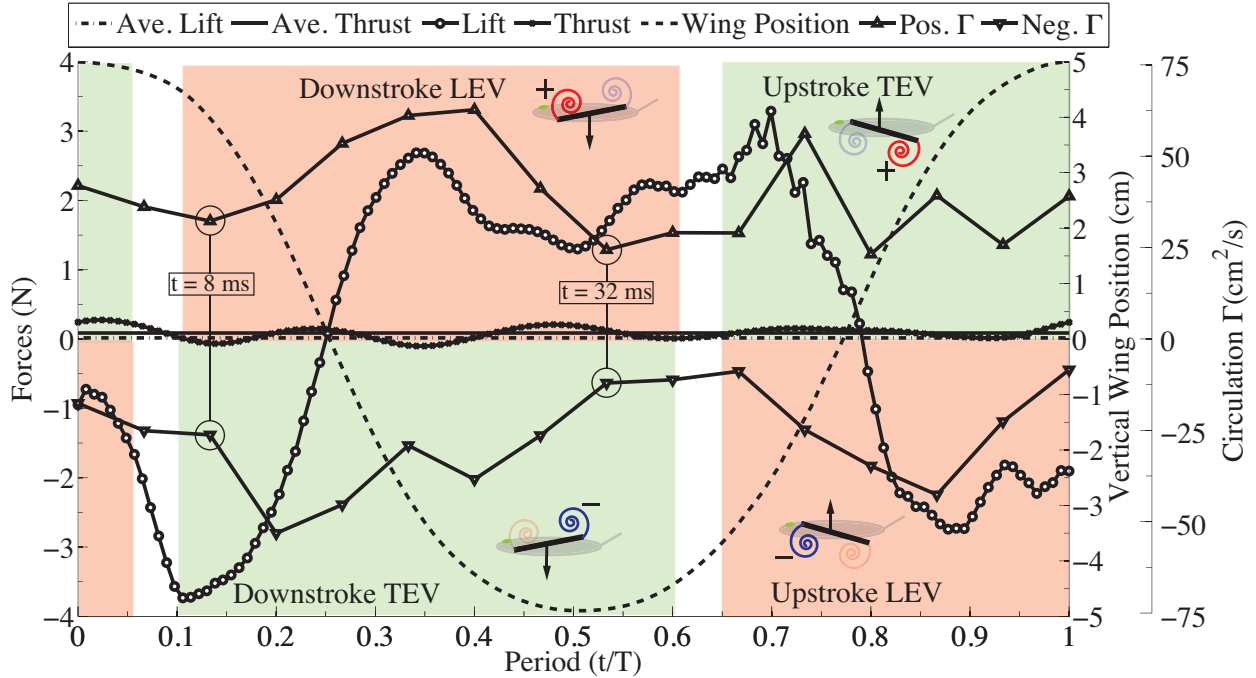
Figure 3.15: Lift and thrust measurements taken using a single-axis load cell as well as positive (red) and negative (blue) circulation Γ calculated from the SAPIV data in Fig. 3.9. The plots represent one flapping period, forces were ensemble averaged over 55 flapping periods (average net lift = 0.014 N and average net thrust 0.084 N). The 95% error for the lift and thrust measurements is on the order of the size of the markers. A graphic of the MAV wing shows the LEV and TEV locations and direction for each stroke. The downstroke LEV and TEV can be observed in Fig. 3.9 from $t = 8 - 28$ ms and the upstroke LEV and TEV from $t = 32 - 52$ ms.

physically observed in Figures 3.9 and 3.12. The positive LEV can be seen growing in size and magnitude at t = 20 - 24 ms and then decreasing and detaching at t = 28 - 32 ms (Figs. 3.9 and 3.12), corresponding to the first peak in positive circulation (t/T = 0.4 in Fig. 3.15). The negative TEV can also be seen growing at t = 8 - 12 ms and then detaching and subsequently decreasing at t = 16 - 20 ms (Figs. 3.9 and 3.12), corresponding to the first peak in negative circulation (t/T = 0.2 in Fig. 3.15).

In both the upstroke and downstroke the TEV detaches first, as witnessed both with the TEV peaks occurring before the LEV peaks in Figure 3.15, and in the vorticity plots in Figures 3.9 and 3.12. The detaching of the TEV and LEV is most easily observed in the higher resolution 2D PIV data in Figure 3.12 at t = 16 - 20 ms and t = 28 - 32 ms, respectively.

The weight of the MAV is 0.128 N using the load cell. By taking the average force over the entire flapping period, the net lift and net thrust (less the weight of the MAV) were determined

to be 0.014 ±0.002 N and 0.084 ±0.001 N with 95% confidence, respectively. This translates to a net lift force 10.98% greater than the weight of the MAV and a net thrust force 65.9% greater than the weight of the MAV.

The lift force was validated by observing the flight behavior after attaching a 0.0098 N weight and then a 0.0196 N weight. With no added weight to the MAV, the flight path had a vertical velocity component, congruent with the net lift force observed in the lift force measurements. When the 0.0098 N weight was added, the flight path was nearly level, and thus the vertical velocity component was reduced to near zero. When the 0.0196 N weight was added, the flight path was downward resulting in a negative vertical velocity component and the forces generated by the MAV could no longer support the total mass, demonstrating that the average lift force was indeed between 0.0098 N and 0.0196 N.

Force Uncertainty

In Figure 3.15, the 95% confidence intervals are on the order of the size of the markers for the lift and thrust force measurements. The intervals increased as the force measurement increased in distance from 0 N. This error was due to slight variations between each flapping period. Upon inspection, it appeared that the minimum and maximum peaks oscillated between a larger and smaller peak value every flapping period. Because the oscillation of force values between flapping periods occurred in the peaks, the error reported was greater in the peaks than in the measurements near 0 N. The greatest variation occurred when $t/T = 0.867$ where the lift force was 0.641 ± 0.004 N. The least uncertainty occurred at $t/T = 0.560$ where the lift force was 0.002 ± 0.0089 N. A correlation between the flow structures and the measured peak values could be studied in later experiments.

3.5   Conclusion

This research explored the use of 3D, time-resolved, Synthetic Aperture PIV in measuring flow velocities on an insect in free flight and a MAV in tethered flight. Fifty image pairs of the butterfly during takeoff were collected and analyzed. The butterfly was extracted from the PIV images and then reconstructed to form the visual hull of the butterfly in the volumetric particle

field. Several time steps during a downstroke and during an upstroke were analyzed. Leading and trailing edge vortices are seen during the downstroke in agreement with previously published studies.

The vortical structures on the MAV were observed using both SAPIV and 2DPIV. XY-plane slices show evidence of span-wise flow in both positive and negative directions, with higher magnitudes within the LEV and TEV. The 3D vorticity plots and 2D slice vorticity plots show the three-dimensional nature of the LEV and TEV. The 2DPIV plots and the 2D slices from the 3D data show general agreement in the structure and behavior of the flow around the flapping wing. The peaks and valleys in the calculated positive and negative circulation show agreement with the peaks and valleys of the measured lift force data. Further work can be done to study the expected span-wise flow using smaller search volumes and larger experimental volumes to reduce air circulation within the acrylic observation tank.

Multiple viewpoints used in SAPIV allow for the ability to see around partial occlusions, including high seeding densities. SAPIV is able to reconstruct 3D velocity fields in time with large spatial regions of interest. The whole-field nature of the velocity fields allows for analysis of flow characteristics not rectified with the camera axes. In comparison with other 3D methods, SAPIV is competitive with the state of the art. This technique is able to measure larger depths than tomographic PIV and can use comparable seeding densities. Furthermore, SAPIV can accommodate similar volumes to and higher seeding densities than holographic PIV, defocusing DPIV, and PTV [16]. One of the drawbacks of using SAPIV in an application requiring high-speed data collection is the overall cost of the system since 8 high-speed cameras are required.

The use of SAPIV to measure fluid flow velocities and reconstruct the visual hull around an insect in free flight and an MAV in tethered flight is feasible and can be useful in elucidating the complex and unsteady nature of this flight regime especially when synchronized with force measurement data.

3.6 Acknowledgements

CHAPTER 4.   FORCE VECTORS

Normal Vectors representing the plane parallel to the MAV wing and the circulation on the MAV wing were created and used to find the lift and thrust contributions of the 3D circulation generated by the LEV and TEV. It has been observed that the LEV and TEV contribute to the lift and thrust forces [2, 4, 5]

4.1   Normal Vector Generation

The normal vectors for each time step were generated by identifying a best fit plane that was parallel to the cores of the LEV and TEV in each time step. By generating a plane that was parallel to the cores of the LEV and TEV, the normal vector to the plane would represent the direction of the force generated by the two vorticies. These normal vectors could then be decomposed into their respective lift and thrust components for comparison with the measured lift and thrust from the force gauge experiments.

To draw the plane of the normal vector, the locations of the LEV and TEV cores needed to be identified. The process of creating the normal vector is shown in Figure 4.1. As the LEV and TEV were often the locations of the maximum and minimum vorticity, the maximum and minimum vorticity values in each time step could be used to locate the cores of the LEV and TEV. The LEV and TEV extended in the z direction. Thus, a searching algorithm was used to find the x and y locations of the cores of the LEV and TEV on each xz plane. The x and y coordinates were retained for the first (near the wing tip) and last (near the base of the wing) xy planes ($z = 21$ mm and $z = 149$ mm, respectively). This resulted in two sets of two points - one set for the LEV and one set for the TEV (Figure 4.1(a)). A line drawn through a set of points would thus represent the line through the core of either the LEV or TEV.

The maximum vorticity value locations on the xz planes represented the LEV core during the downstroke and the TEV core during the upstroke. The minimum vorticity value locations
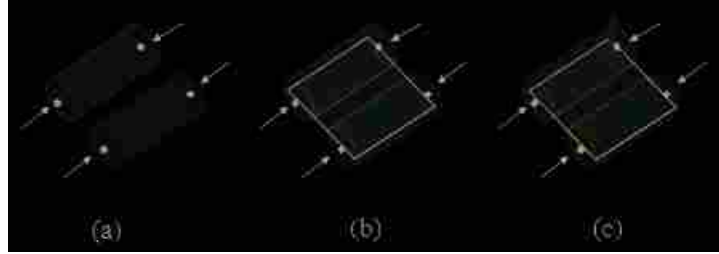
Figure 4.1: A normal vector was determined for each timestep, representing the direction of the force normal to the LEV and TEV. The vortex cores were identified by finding the maximum and minimum vorticity values on the xy planes (a). A least-squares regression found a best fit plane through the 4 points, representing a plane parallel to the vortex cores (b). A unit direction vector was generated normal to the vortex plane and pointing up and away from the top of the wing (c).

on the xz planes represented the TEV core during the downstroke and the LEV core during the upstroke. During transitions between the upstroke and downstroke, the new LEV and TEV were not necessarily the sources of maximum and minimum vorticity. Each timestep was inspected for correct identification of the LEV and TEV cores by comparing the sets of points to the approximate location of the wing. If the algorithm incorrectly identified a vortex that was not attached to the wing as the LEV or TEV, the locations were moved to the vortices attached to the wing to reflect the true LEV and TEV locations at that time step.

A plane parallel to the vortex cores was found by performing a least-squares regression on the 4 points identifying the LEV and TEV cores to find the best fit plane (Figure 4.1(b)), that is, 2 pairs of points identifying the vortex core axes, and a best fit plane between the two axes. A unit direction vector normal to the plane was then generated (Figure 4.1(c)). The direction of the normal vector for each time step was chosen arbitrarily by the least squares regression algorithm. All normal vectors were subsequently signed so that the vectors pointed up and away from the top of the wing. This provided uniformity to the normal vectors, and the sign of the circulation would then determine the direction of the force generated by the LEV and TEV.

Figure 4.2 shows the resulting plane and normal vector for t=12 ms, which is during the downstroke (in the downstroke the leading edge of the wing leads the trailing edge). The point identifying the maximum vorticity location on the front xz plane can be seen in the center of the left vortex, or the LEV. The point identifying the minimum vorticity location on the front xz plane
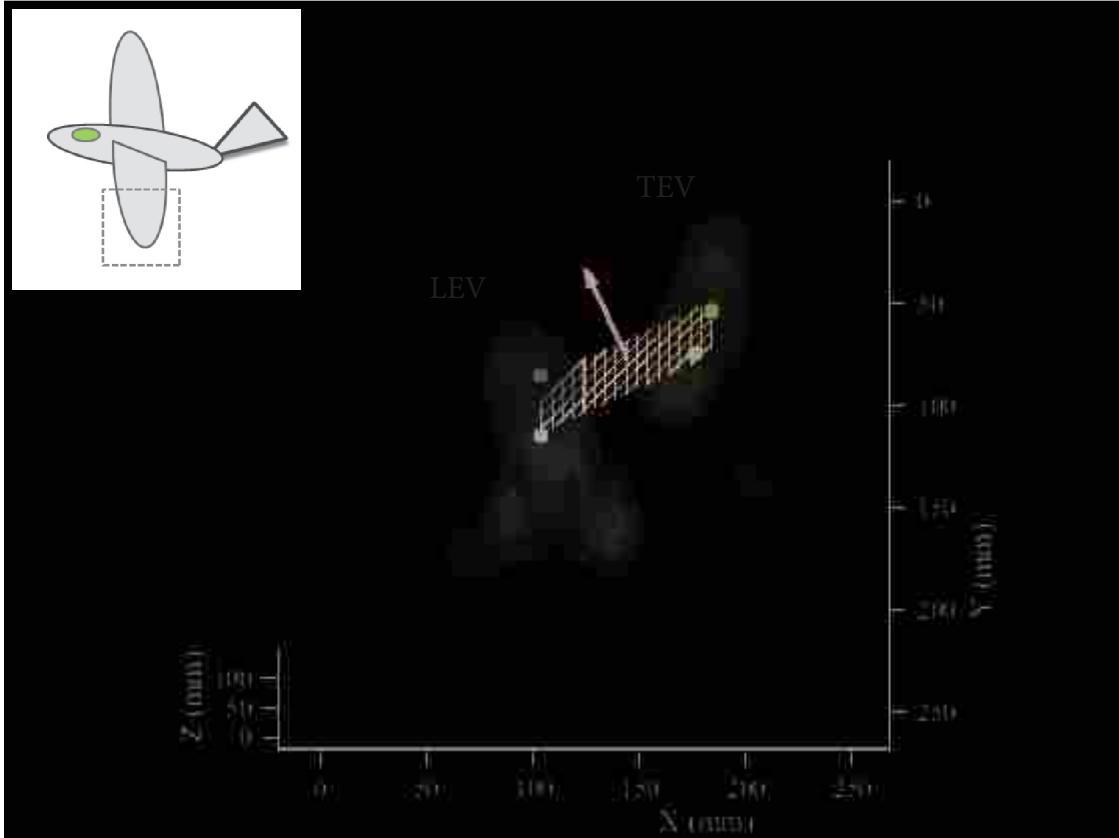
Figure 4.2: The plane parallel to the LEV and TEV cores and normal vector for time step t=12 ms. The LEV and TEV are also plotted. The maximum and minimum vorticity locations for the front *xz* plane, representing the LEV and TEV cores, respectively, can be seen on the left and right corners of the plotted plane, respectively. The MAV wing is located just below the plane and is in the middle of the downstroke. The normal vector points up and away from the top of the wing.

can be seen in the center of the right vortex, or the TEV. The other two points can be seen on the back *xz* plane, appearing above the front *xz* plane points.

Plots of all 16 planes and normal vectors with the accompanying LEVs and TEVs can be seen in Figure 4.3. The downstroke occurs from t=0 ms to t=28 ms. The upstroke occurs from t=32 ms to t=60 ms. The plane parallel to the vortex cores can be seen intersecting the LEV and TEV in each time step. The normal vector in each timestep was directed upward and away from the top of the wing. The wing would be located just below the vortex plane in the downstroke and just above the vortex plane in the upstroke.

Time steps 56 ms and 60 ms can be seen to significantly vary from the previous time steps in Figure 4.3. The algorithm used for locating the LEV and TEV did not output location points
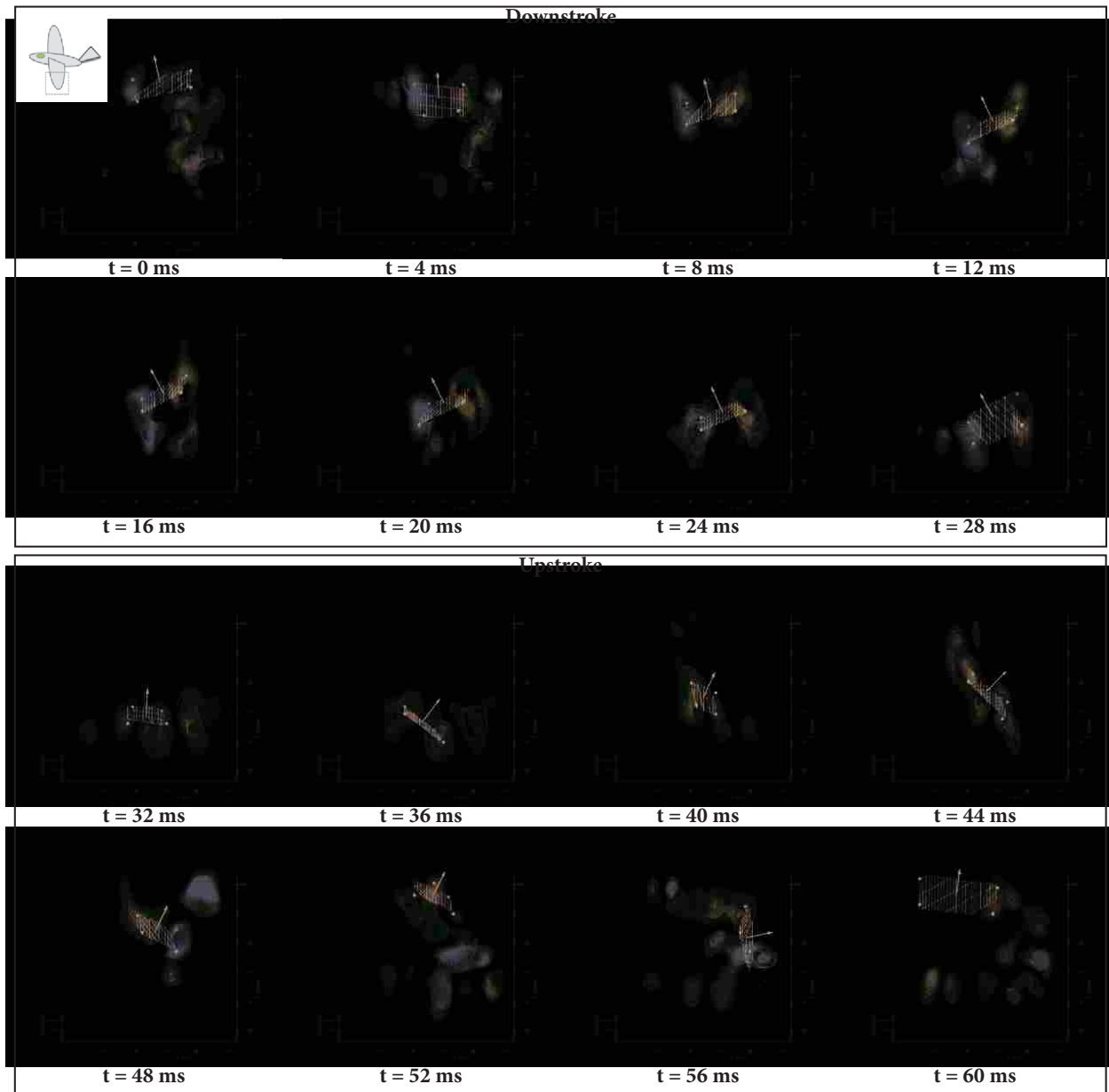
Figure 4.3: Plots of the normal vectors for all 16 time steps with the associated LEVs and TEVs. The downstroke occurs from t = 0 ms to t = 28 ms. The upstroke occurs from t = 32 ms to t = 60 ms. The plotted plane can be seen intersecting the LEV and TEV in each time step. The normal vector can also be seen pointing up and away from top of the wing. The wing would be located just below the planes in the downstroke and just above the planes in the upstroke. Time steps at 56 ms and 60 ms vary significantly from the other time steps and are not considered accurate.

50

that corresponded to the actual LEV and TEV, and the true LEV and TEV could not be visually located in the flow field, either. The wing was partially outside the laser illuminated volume, and there was a significant amount of vorticity visible throughout the entire volume in each of those time steps. These factors hindered locating of the LEV and TEV cores in time steps t = 56 ms and t = 60 ms and the normal vectors generated were not considered accurate.

4.2   Vector Decomposition

The normal vectors for each time step were decomposed into their unit vector components. Figure 4.4 shows the x, y, and z unit vector components of the normal vectors for each timestep with the unit vectors plotted below. The first 8 points represent downstroke time steps, and the remaining 8 points represent upstroke time steps, as illustrated by the white and grey boxes on the plot, respectively. The y component is negative (pointing upwards from the MAV according to the frame of reference) the entire flapping period. The x component is negative (pointing towards the front of the MAV) during the downstroke and positive (pointing towards the tail of the MAV) during the upstroke. The z component oscillates around zero (towards the wing tip and towards the body of the MAV) and never exceeds 0.16 in magnitude.

The plots in Figure 4.4 can be explained by considering what is physically occuring during the flapping period. As the MAV wing moves up and down, the angle of attack of the wing never exceeds 90 degrees, so the top side of the wing never points downward. This explains why the y component of the unit vector of every time step is always negative, or pointing upwards according to the frame of reference shown in the upper right corner of Figure 4.4. While the angle of attack never exceeds 90 degrees, it does oscillate between being negative during the downstroke, and positive during the upstroke. This explains why the x component of the unit vectors is negative during the downstroke and positive during the upstroke. Negative angles of attack result in a negative x component, and positive angles of attack result in a positive x component. The affect of the sign of the angle of attack can also be seen in the unit vectors plotted below the components plot. During the downstroke, the vectors are pointing towards the front of the MAV. During the upstroke, the vectors point towards the tail of the MAV.

The small oscillations in the z component observed in Figure 4.4 can be explained by the slight differences in the y and x coordinates of the vortex cores on the front and back z planes. As
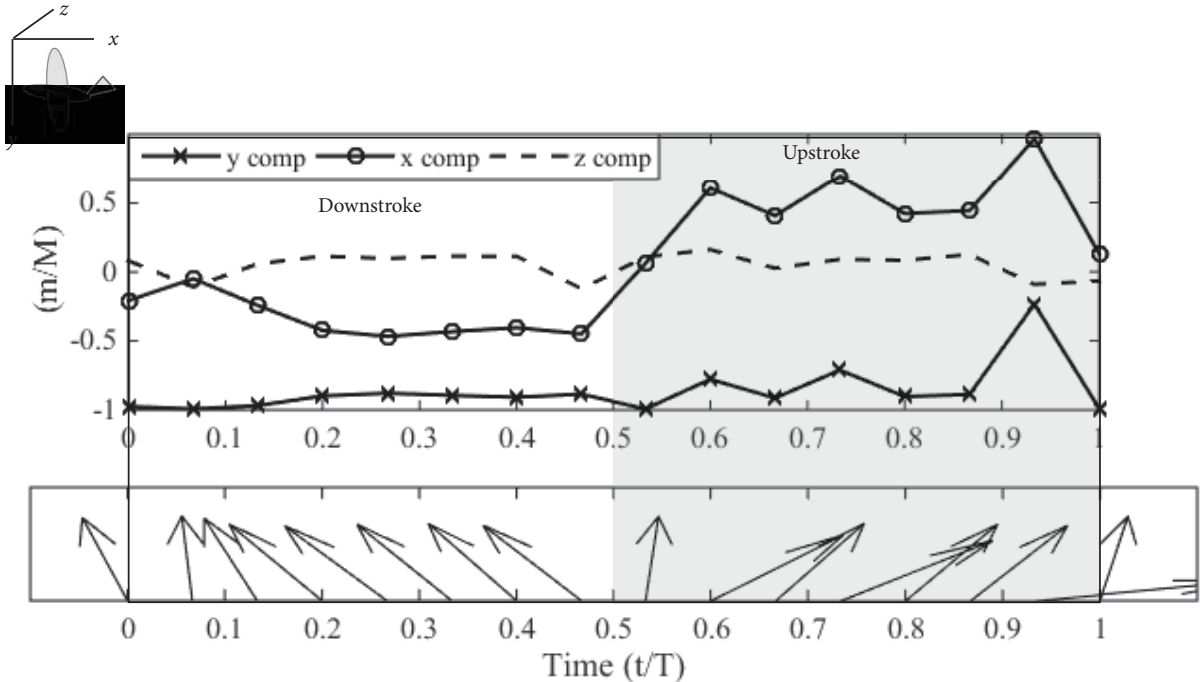
Figure 4.4: The change in time of the x, y, and z components from the unit normal vectors of the vortex planes with the unit vectors plotted below. The unit vector components represent the vector normal to the top side of the MAV wing. The first 8 points represent the downstoke, and the last 8 points represent the upstroke. The y component remains negative (upward in the frame of reference) through the entire flapping period. The x component begins negative (forward towards the front of the MAV) in the downstroke and switches to positive (backward towards the tail of the MAV) in the upstroke. The magnitude of z never exceeds 0.16, and is symmetric about the MAV body axis, thus any force would net zero over the entire wing span of the MAV.

the wing tip moves downward during the downstroke, the LEV and TEV are attached to the wing and rotate downward with the wing tip. As the wing tip moves upward during the upstroke, the LEV and TEV likewise rotate upward. There is also variations in the x and y coordinates of the LEV and TEV cores due to the resolution of the flow field measurements.

It is important to note that the z component is small compared to the x and y components. It should also be noted that any forces generated in the z direction would be symmetric about the MAV body axis and therefore net zero. If the z direction forces were not symmetric, the MAV would strafe to the left or right as it flew, as if sliding on the air.

52

4.3 Force Gauge and Flow Field Comparison

The unit vector components for each timestep allowed for calculation of lift and thrust estimates from the SAPIV flow field data. The circulation at each time step was calculated using the method outlined in Chapter 3. The total circulation (the sum of the positve and negative circulation) instead of the positive and negative circulation was calculated at each xz plane along the span of the MAV wing using 35% of maximum vorticity threshold, matching the 35% threshold used in all of the previous figures and previous circulation calculations. This percent cut-off below maximum vorticity allows the amount of vorticity included in the circulation calculations to be defined by the flow field data, rather than an arbitrary assignment of an area of inclusion [38]. The force normal to the wing was calculated using the Kutta-Joukowski theorem

$$L' = \rho v \Gamma$$

where ρ is the air density (1.044 kg/m^3), v is the freestream velocity (free flight $v = 1$ m/s), Γ is the circulation (calculated from the flow field), and L' is the force per unit length of the wing span at each xz plane. A stepwise approximation for circulation along the span of the wing was used. This means the force per unit length at each xz plane was applied to the distance along the span to the next xz plane ($dz = 0.021$ m). The Kutta-Joukowski theorem equation was thus modified to be

$$L = \rho v \Delta z \sum \Gamma$$

. This provided a force calculated from the 3D circulation measurements instead of using the circulation calculated at a single xz plane and applying it to the entire wing.

Figure 4.5 shows a plot of the positive, negative, and total circulation, summed along the wing on the left plot axis. The normal force is also plotted on the right plot axis. The normal force was calculated using the total circulation at each xz plane. The normal force follows the total circulation because of the direct correlation between the normal force and circulation, as shown in the Kutta-Joukouski theorem. Another observation is that the normal force exhibits two peaks, each at times when the positive circulation peaks at t/T = 0.2 and t/T = 0.87. Also, the normal
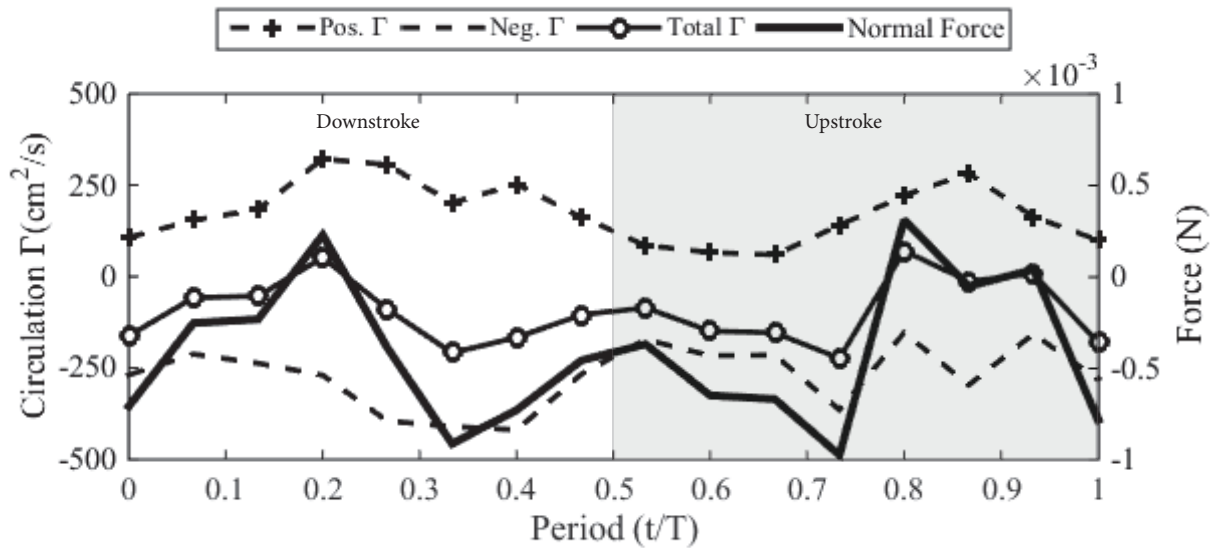
Figure 4.5: A plot showing the negative, positive, and total combined circulation (negative + positive), as well as the normal force associated with the circulation. The first 8 points represent the downstoke, and the last 8 points represent the upstroke. The normal force follows the total circulation due to the correlation between the normal force and circulation. The normal force exhibits two peaks, at times t/T = 0.2 and t/T = 0.87 when the positive circulation also peaks. The normal force contains minimums at times t/T = 0.32 and t/T = 0.73 when the negative circulation peaks.

force contains two valleys, each at times when the negative circulation peaks at t/T = 0.32 and t/T = 0.73.

After finding the normal force generated by the 3D circulation measurements, the unit direction vector components were applied to the normal force to calculate the lift and thrust forces generated by the circulation. Figure 4.6 shows the thrust force calculated from the circulation measurements plotted agains the measured thrust force from the force gauge experiments. The forces were normalized for comparison of trends. The plots in Figure 4.6 do not show much in immediate similarities. While the measured thrust force exhibits a pronounced oscillation, an oscillating pattern in the calculated circulation thrust force is not as clear. This could be due to the unit direction vector being based off of vortex core locations that may have some error due to the resolution, or due to forces that could be acting on the MAV from the wake that could not be measured due to the size constraints of the volume of interest. Because the thrust component is
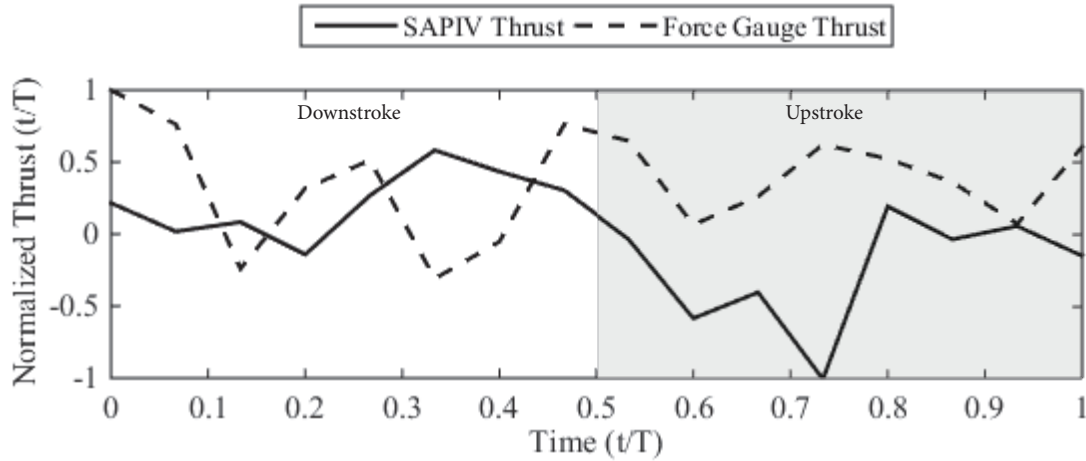
Figure 4.6: A plot showing the normalized calculated thrust force from circulation plotted against the measured thrust force from the force gauge. The is an obvious oscillation pattern in the measured thrust force data. An oscillating pattern is less clear in the calculated thrust force data. Possible reasons for differences in the claculated and measured thrust forces coud be due to the resolution of the SAPIV data as well as wake effects that could not be imaged due to sized constraints of the volume of interest. The thrust is subject to greater sensitivity to error in the calculated angle of attack at small angles ($<$ 20 deg).

related to the unit vector through the sine of the angle of attack of the wing, the thrust component is sensitive to error in the calculated angle of attack from the vortex cores for small angles of attack ($<$ 20 deg).

The measurement of sensitivity of the lift and thrust components of the normal vector helps to explain part of the discrepancy between the measured and calculated thrust forces. The lift component corresponds to the cosine of the angle of attack. The lift component corresponds to the sine of the angle of attack. At an angle of attack of 20 deg, an error of ± 1 deg results in $\pm 0.65\%$ error in the lift component and $\pm 4.78\%$ in the thrust component. At an angle of attack of 10 deg, an error of ± 1 deg results in $\pm 0.32\%$ error in the lift component and $\pm 9.88\%$ in the thrust component. At an angle of attack of 5 deg, an error of ± 1 deg results in $\pm 0.17\%$ error in the lift component and $\pm 19.93\%$ in the thrust component.

Figure 4.7 shows the lift force calculated from the 3D circulation measurements plotted against the measured lift force from the force gauge experiments. The forces were normalized for comparison of trends. It is immediately apparent that the measured lift force and calculated lift
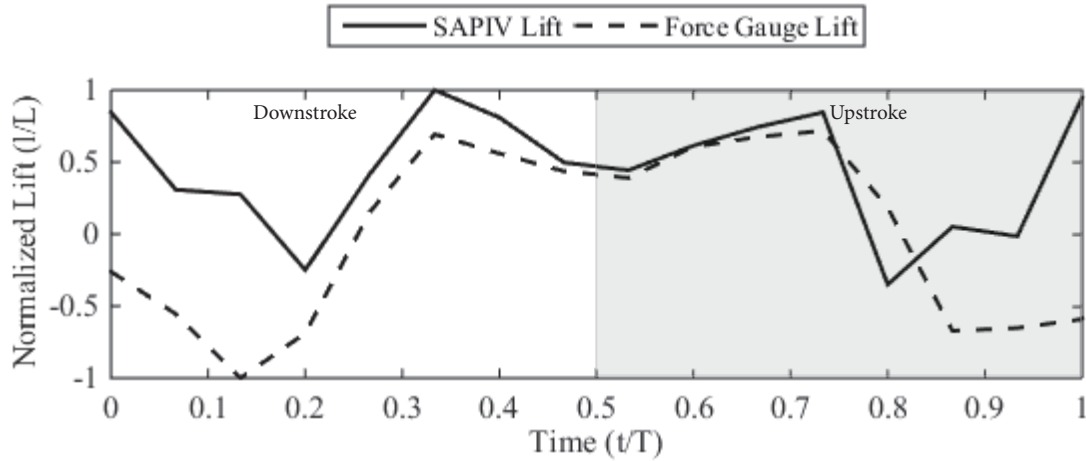
Figure 4.7: The normalized calculated lift force from circulation plotted against the normalized measured lift force from the force gauge. Both force plots exhibit a lag in the lift force sign change during the downstroke (on the left) and upstroke (on the right). This is due to the LEV and TEV from the previous half stroke remaining attached while the new LEV and TEV grow, with the old LEV and TEV eventually being shed into the wake, witnessed by the rapid sign change in the lift force halfway into the downstroke and halfway into the upstroke.

force from the circulation measurements share similar profiles. During the downstroke on the left side of Figure 4.7, a downward slope is observed in the lift forces, followed by a slope reversal and sign change in the lift force. During the upstroke on the right side of the figure, the lift force begins positive, then rapidly becomes negative halfway through the half stroke. The sign change in the lift forces lags behind the downstroke to upstroke transition by four time steps.

The apparent lag in lift force sign change during the downstroke and upstroke could be explained by the behavior of the vorticies around the wing. At the beginning of the downstroke, the LEV and TEV from the upstroke have not been shed into the wake and are still contributing to the circulation of the wing. As the new LEV and TEV grow and the old LEV and TEV are shed into the wake, the circulation direction reverses suddenly, as seen by the rapid sign change of the lift force on the left side of Figure 4.7. A similar observation of old and new LEV and TEV interactions occurs during the transition from downstroke to upstroke, as shown in the rapid sign change of the lift force on the right side of Figure 4.7. Thus, there is a lag in the lift force sign change due to LEV and TEV of the previous half stroke remaining attached and traveling along the wing in the first four timesteps of each half stroke.

CHAPTER 5.   CONCLUSIONS

This research explored the use of 3D, time-resolved, Synthetic Aperture PIV in measuring flow velocities on a MAV in tethered flight. The vortical structures on the MAV were observed using both SAPIV and 2DPIV. Changing cross sections of the LEV and TEV show evidence of spanwise flow in the direction of the wing tip. The 3D vorticity plots and 2D slice vorticity plots show the three-dimensional nature of the LEV and TEV. And finally, the 2DPIV plots and the 2D slices from the 3D data show general agreement in the structure and behavior of the flow around the flapping wing.

The use of Synthetic Aperture Particle Image Velocimetry to measure fluid flow velocities and reconstruct the visual hull around a MAV in tethered flight is feasible and can be useful in elucidating the complex and unsteady nature of this flight regime. This study has presented results showing the measurement of leading and trailing edge vortices and agree with data previously published by Ol et al. [37].

By measuring the lift and thrust forces generated by the MAV using a force gauge, comparisons could be made between the measured force and the calculated force from the circulation found through SAPIV flow field measurements. The use of the LEV and TEV vortex cores allows the generation of a plane with a vector normal to the wing and the LEV and TEV. The decomposition of the normal vector allowed for the calculation of the lift and thrust generated by the circulation around the wing. The comparisons between the measured and calculated forces showed particularly good agreement in the case of the lift forces.

This work represents one of the first times that 3D, time-resolved flow fields have been used to calculate the lift and thrust generated by a flapping wing. In particular, this is the first time that the autor knows of that circulation has been calculated at spaced intervals along a flapping wing using instantaneous 3DPIV as opposed to phased average 2DPIV and 3DPIV.

Further work can be done in improving the results by exploring seeding techniques to produce denser particle seeding. Improved force data can be calculated in the future by producing multiple runs whose results can be averaged, just as the measured force data was averaged. Future studies will also benefit from being performed in a wind tunnel where a free stream velocity matched to the free flight velocity of the MAV can be generated the better simulate real world conditions as well as speed up the shedding of vorticies to reduce the impact of excessive vorticity in the volume of interest.

REFERENCES

[1] Shyy, W., Aono, H., Chimakurthi, S. K., Trizila, P., Kang, C. K., Cesnik, C. E. S., and Liu, H., 2010. "Recent progress in flapping wing aerodynamics and aeroelasticity." *Progress in Aerospace Sciences,* **46**(7), 10, pp. 284–327. ii, 1, 2, 19

[2] Clemons, L., Igarashi, H., and Hu, H., 2010. "An experimental study of unsteady vortex structures of a piezoelectric flapping wing." In *AIAA Aerospace Sciences Meeting Including the New Horizons Forum and Aerospace Exposition*, no. AIAA 2010-1025. 1, 19, 47

[3] Rayner, J. M. V., 1979. "Vortex theory of animal flight - 1. the vortex wake of a hovering animal.." *Journal of Fluid Mechanics,* **91**(pt), pp. 697–730. 1

[4] Birch, J. M., Dickson, W. B., and Dickinson, M. H., 2004. "Force production and flow structure of the leading edge vortex on flapping wings at high and low reynolds numbers." *Journal of Experimental Biology,* **207**(7), pp. 1063–1072. 1, 2, 5, 47

[5] van den Berg, C., and Ellington, C. P., 1997. "The vortex wake of a "hovering" model hawkmoth." *Philosophical Transactions of the Royal Society of London Series B-Biological Sciences,* **352**(1351), pp. 317–328. 1, 47

[6] Ellington, C. P., van den Berg, C., Willmott, A. P., and Thomas, A. L. R., 1996. "Leading-edge vortices in insect flight." *Nature,* **384**(6610), pp. 626–630. 2

[7] Bomphrey, R. J., 2006. "Application of digital particle image velocimetry to insect aerodynamics: Measurement of the leading-edge vortex and near wake of a hawkmoth." *Experiments in Fluids,* **40**(4), pp. 546–554. 2, 20

[8] Poelma, C., Dickson, W., and Dickinson, M., 2006. "Time-resolved reconstruction of the full velocity field around a dynamically-scaled flapping wing." *Experiments in Fluids,* **41**(2), pp. 213–225. 2, 5, 20

[9] Taira, K., and Colonius, T., 2009. "Three-dimensional flows around low-aspect-ratio flat-plate wings at low reynolds numbers." *Journal of Fluid Mechanics,* **623**, pp. 187–207. 3, 20

[10] George, R. B., Colton, M. B., Mattson, C. A., and Thomson, S. L., 2012. "A differentially driven flapping wing mechanism for force analysis and trajectory optimization." *International Journal of Micro Air Vehicles,* **4**(1), pp. 31–49. 3

[11] InteractiveToyConcepts, 2007. ifly vamp manual `http://www.interactivetoy.com/IATC1011/home/manuals/iFly-Vamp_EN.pdf`. 3

[12] van den Berg, C., and Ellington, C. P., 1997. "The three-dimensional leading-edge vortex of a 'hovering' model hawkmoth." *Philosophical Transactions of the Royal Society of London Series B-Biological Sciences,* **352**(1351), pp. 329–340. 4

[13] Raffel, M., Willert, C., Wereley, S., and Kompenhans, J., 2007. *Particle Image Velocimetry A Practical Guide.*, 2 ed. Springer-Verlag Berlin Heidelberg. 4

[14] Lu, Y., and Shen, G., 2008. "Three-dimensional flow structures and evolution of the leading-edge vortices on a flapping wing." *Journal of Experimental Biology,* **211**(8), pp. 1221–1230. 5, 6, 20

[15] Bomphrey, R. J., Henningsson, P., Michaelis, D., and Hollis, D., 2012. "Tomographic particle image velocimetery of desert locust wakes: instantaneous volumes combine to reveal hidden vortex elements and rapid wake deformation." *Journal of The Royal Society Interface,* **9**(77), September, pp. 3378–3386. 5, 6, 20, 33, 39

[16] Belden, J., Truscott, T., Axiak, M. C., and Techet, A. H., 2010. "Three-dimensional synthetic aperture particle image velocimetry." *Measurement Science and Technology,* **21**(12), p. 125403. 6, 11, 12, 21, 24, 25, 26, 33, 45

[17] Langley, K. R., Hardester, E., Thomson, S. L., and Truscott, T. T., 2014. "Three-dimensional flow measurements on flapping wings using synthetic aperture piv." *Experiments in Fluids,* **55**(10). 7

[18] Thomson, S. L., 2004. Direct linear transformation (dlt) `https://me363.byu.edu/sites/ me363.byu.edu/files/userfiles/5/DLTNotes.pdf`. 17

[19] Bomphrey, R., 2011. "Advances in animal flight aerodynamics through flow measurement." *Evolutionary Biology,* **39**(1), pp. 1–11. 20

[20] Henningson, P., and Bomphrey, R. J., 2011. "Time-varying span efficiency through the wingbeat of desert locusts." *Journal of The Royal Society Interface.* 20

[21] Bomphrey, R. J., Lawson, N. J., Harding, N. J., Taylor, G. K., and Thomas, A. L. R., 2005. "The aerodynamics of manduca sexta: digital particle image velocimetry analysis of the leading-edge vortex." *Journal of Experimental Biology,* **208**(6), p. 1079. 20

[22] Bomphrey, R. J., Taylor, G. K., Lawson, N. J., and r. Thomas, A. L., 2006. "Digital particle image velocimetry measurements of the downwash distribution of a desert locust schistocerca gregaria." *Journal of The Royal Society,* **3**(7), pp. 311–317. 20

[23] Fuchiwaki, M., Kuroki, T., Tanaka, K., and Tababa, T., 2013. "Dynamic behavior of the vortex ring formed on a butterfly wing." *Experiments in Fluids,* **54**. 20, 30, 32

[24] Mazaheri, K., and Ebrahimi, A., 2010. "Experimental study on interaction of aerodynamics with flexible wings of flapping vehicles in hovering and cruise flight." *Archive of Applied Mechanics,* **80**(11), pp. 1255–1269. 20

[25] David, L., Jardin, T., Braud, P., and Farcy, A., 2012. "Time-resolved scanning tomography piv measurements around a flapping wing." *Experiments in Fluids,* **52**(4), pp. 857–864. 20

[26] Mendelson, L., and Techet, A. H., 2013. "3d synthetic aperture piv of a swimming fish." In *10TH International Symposium on Particle Image Velocimetry - PIV13*, J. Westerweel, ed. 21

[27] Belden, J., Ravela, S., Truscott, T. T., and Techet, A., 2012. "Three-dimensional bubble field resolution using synthetic aperture imaging: application to a plunging jet." *Experiments in Fluids,* **52**(6), June, pp. 839–861. 21

[28] Otsu, N., 1975. "A threshold selection method from gray-level histograms." *Automatica,* **11**(285-296), pp. 23–27. 24

[29] Adhikari, D., and Longmire, E., 2012. "Visual hull method for tomographic piv meassurement of flow around moving objects." *Experiments in Fluids,* **53**, pp. 943–964. 24

[30] Svoboda, T., Martinec, D., and Pajdla, T., 2005. "A convenient multi-camera self-calibration for virtual environments." *PRESENCE: Teleoperators and Virtual Environments,* **14**(4), August, pp. 407–422. 26

[31] Hartley, R., and Zisserman, A., 2010. *Multiple View Geometry in Computer Vision.*, 2 ed. Cambridge University Press, The Edinburgh Building, Cambridge CB2 8RU, UK. 26

[32] Luff, J., Douillard, T., Rompage, A., Linne, M., and Hertzberg, J., 1999. "Experimental uncertainties associated with particle image velocimetry (piv) based vorticity algorithms." *Experiments in Fluids,* **26**. 26, 34

[33] Bimbard, G., Kolomenskiy, D., Bouteleux, O., Casas, J., and Godoy-Diana, R., 2013. "Force balance in the take-off of a pierid butterfly: relative importance and timing of leg impulsion and aerodynamic forces." *The Journal of Experimental Biology,* **216**(18), pp. 3551–3563. 27

[34] Srygley, R. B., and Thomas, A. L. R., 2002. "Unconventional lift-generating mechanisms in free-flying butterflies." *Nature,* **420**(6916), p. 660. 33

[35] Scarano, F., and Poelma, C., 2009. "Three-dimensional vorticity patterns of cylinder wakes." *Experiments in Fluids,* **47**, pp. 69–83. 33

[36] Taylor, G. K., Nudds, R. L., and Thomas, A. L., 2003. "Flying and swimming animals cruise at a strouhal number tuned for high power efficiency." *Nature,* **425**(6959), pp. 707–711. 34

[37] Ol, M., Dong, H., and Webb, C., 2008. "Motion kinematics vs. angle of attack effects in high-frequency airfoil pitch/plunge." In *38th Fluid Dynamics Conference and Exhibit*, American Institute of Aeronautics and Astronautics. 37, 57

[38] Epps, B., and Techet, A., 2007. "Impulse generated during unsteady maneuvering of swimming fish." *EXPERIMENTS IN FLUIDS,* **43**(5), pp. 691–700. 40, 53

APPENDIX A.   PIV UNCERTAINTY CALCULATIONS

The uncertainty of the 2DPIV and SAPIV measurement was calculated by first calculating the uncertainty in the equipment and method of correlation, u_{calc}, and the particle movement, $u_{settling}$ and $u_{inertia}$. u_{calc} was calculated based on the uncertainty from the particle location on the camera CCD and the uncertainty from the particle location due to the laser and pulse generator timing uncertainty, represented by the first and second terms in the u_calc equation, respectively. The total uncertainty, u_{total}, was calculated using the equations below. The values used for the calculations are included in Table A.1 for the SAPIV uncertainty and Table A.2 for the 2DPIV uncertainty.

$$u_{total} = \sqrt{u_{calc}^2 + u_{settling}^2 + u_{inertia}^2}$$

$$u_{calc} = \sqrt{(\frac{1}{\Delta t}u_d)^2 + (\frac{\bar{u}}{\Delta t}\frac{l}{L})^2(u_{t1}^2 + u_{t2}^2)}$$

$$u_d = \sqrt{(\frac{1}{2}\frac{l}{L})^2 + (\frac{1}{20}\frac{l}{L})^2}$$

$$u_{settling} = \frac{2(\rho_p - \rho_f)a^2 g}{9\mu_f}$$

$$\tau = \frac{2a^2\rho_p}{9\mu_f}$$

$$u_{inertia} = \bar{u} - \bar{u}(1 - e^{\frac{-\Delta t}{\tau}})$$

Table A.1: The variables, definitions, and values used for
the SAPIV uncertainty calculations.

Variable	Definition	Value
u_{total}	Total Uncertainty	0.3243 m/s
u_{calc}	Uncertainty from calculations	0.3141 m/s
$u_{settling}$	Settling velocity of particles	0.0010 m/s
$u_{inertial}$	Uncertainty from particle inertial effects	0.081 m/s
u_d	Uncertainty from distance measurements	1.256e-4 m/s
Δt	Time between laser pulses	0.0004 m/s
$\frac{l}{L}$	Length per pixel	0.00025 m
u_{t1}	Laser timing uncertainty	1e-9 s
u_{t2}	Pulse generator uncertainty	200e-12 s
$\bar{u}$	Average flow velocity	2.87 m/s
ρ_p	Density of particles	25 kg/m^3
ρ_f	Density of fluid	1.23 kg/m^3
μ_f	Viscocity of fluid	1.983e-5 Pa s
a	Particle radius	20 μm
g	Gravity constant	9.81 m/s^2
τ	Time constant	1.14e-4 s

Table A.2: The variables, definitions, and values used for
the 2DPIV uncertainty calculations.

Variable	Definition	Value
u_{total}	Total Uncertainty	0.3181 m/s
u_{calc}	Uncertainty from calculations	0.3141 m/s
$u_{settling}$	Settling velocity of particles	0.0010 m/s
$u_{inertial}$	Uncertainty from particle inertial effects	0.0505 m/s
u_d	Uncertainty from distance measurements	1.256e-4 m/s
Δt	Time between laser pulses	0.0004 m/s
$\frac{l}{L}$	Length per pixel	0.00025 m
u_{t1}	Laser uncertainty	1e-9 s
u_{t2}	Pulse generator uncertainty	200e-12 s
$\bar{u}$	Average flow velocity	1.79 m/s
ρ_p	Density of particles	25 kg/m^3
ρ_f	Density of fluid	1.23 kg/m^3
μ_f	Viscocity of fluid	1.983e-5 Pa s
a	Particle radius	20 μm
g	Gravity constant	9.81 m/s^2
τ	Time constant	1.14e-4 s

APPENDIX B.   FORCE MEASUREMENTS LABVIEW VI'S

The force measurements were acquired using a National Instruments cRIO chassis with a Analog Input Module and Digital Output Module. The camera used to track the wingtip was triggered using the same module.

Two VI's were used for the force data acquisition and camera shutter triggering, a Top Level VI for computer control and user input, and a sequenced VI loaded onto the FPGA of the cRIO chassis for the actual data acquisition and timing.The Top Level VI (Figure B.1) performed three tasks. It initialized the hardware and settings for force acquisition and camera triggering, pulled the acquired data off the cRIO chassis and logged it in a file, and closed out the operations of the cRIO at the end of the expirement.
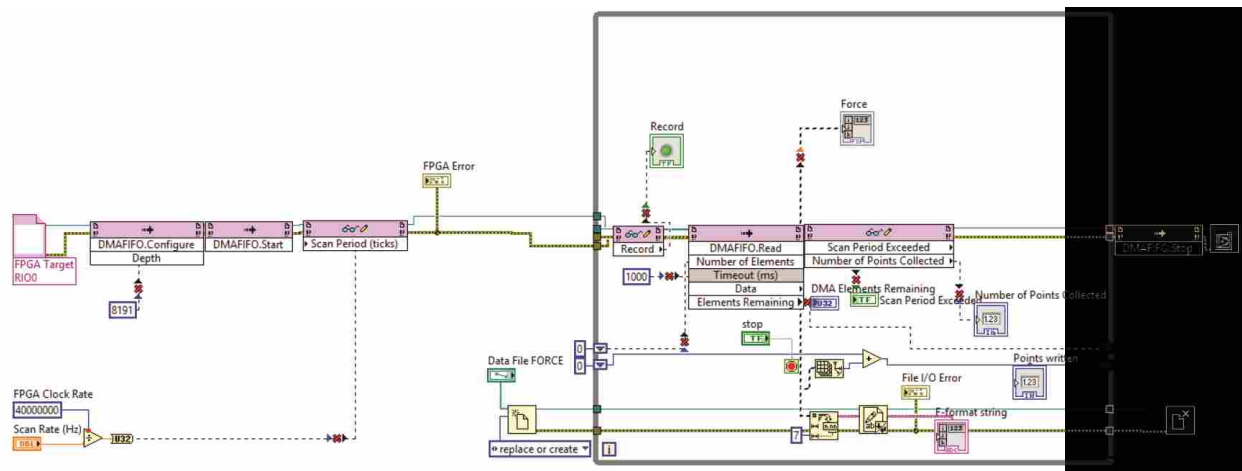

Figure B.1: The Top Level VI initialized the hardware and settings of the experimental setup, read in the data from the cRIO chassis and logged it in a file, and closed out the cRIO at the end of the experiment.

The timing of the force data with the camera trigger required the data acquisition and timing VI to be run from the FPGA card on the cRIO chassis. The Windows operating system does not provide reliable timing beyond 50 ms, and the camera trigger signal required synchronization at

the 0.25 ms level, thus necessitating the use of the FPGA on the cRIO. The VI stored on the FPGA (Figure B.2) performed three tasks. It acquired force data at 4000 Hz, stored the acquired data in a DMAFIFO buffer to allow time for the main computer to read in the data and log it to a file without losing any data points, and generating a synchronized trigger pulse for the camera shutter at 2000 Hz.
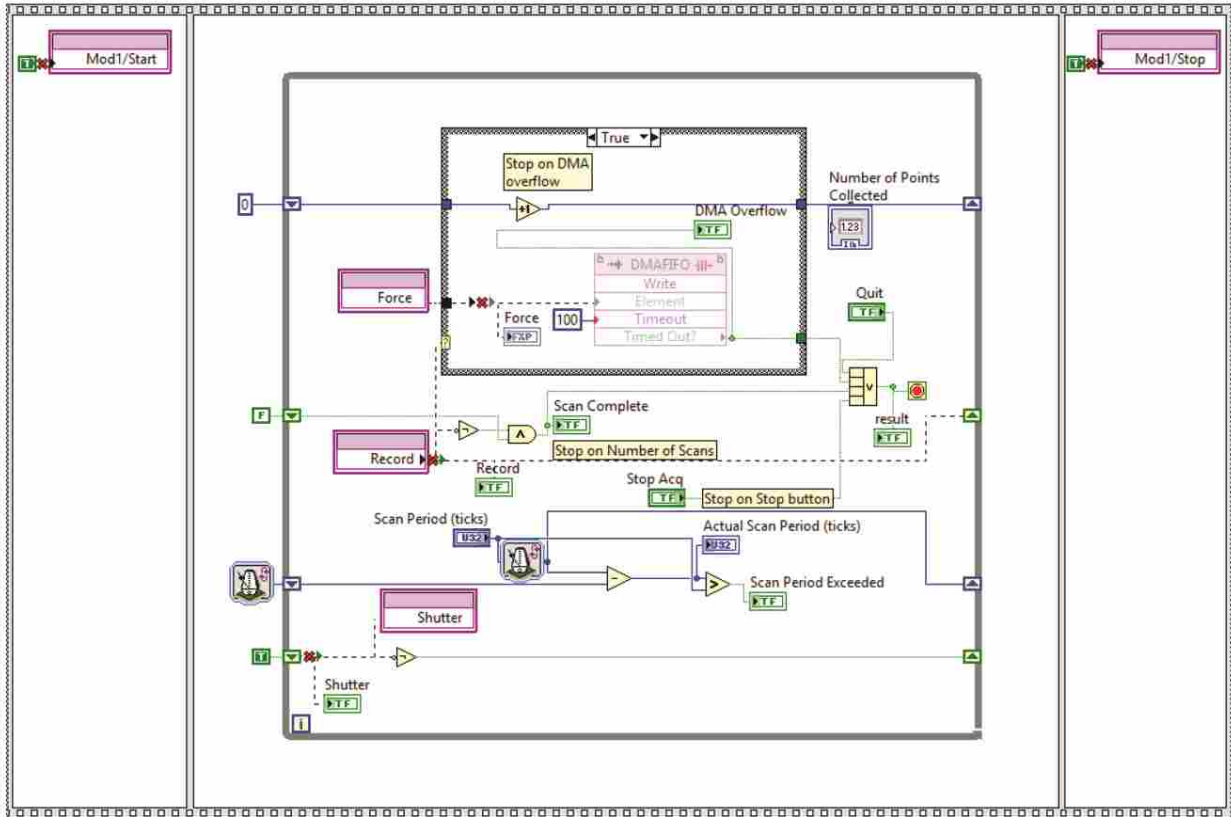

Figure B.2: LabVIEW code was loaded onto the FPGA on the cRIO chassis to provide greater control over the timing of the force measurements and camera shutter triggering. The FPGA performed three tasks. It acquired the force data from the load cell at 4000 Hz, stored the data in a DMAFIFO buffer, and generated a synchronized trigger pulse for the camera shutter at 2000 Hz.